The Thermal Equation of State of (Mg, Fe)SiO_3 Bridgmanite (Perovskite) and Implications for Lower Mantle Structures

Aaron S. Wolf[1,2], Jennifer M. Jackson[2], Przemeslaw Dera[3,4], and Vitali B. Prakapenka[5]

Corresponding author: Aaron S. Wolf, Department of Earth and Environmental Sciences, University of Michigan, 2534 C.C. Little Building, 1100 North University Ave, Ann Arbor, MI 48109, USA. (aswolf@umich.edu)

[1]Department of Earth and Environmental

Abstract. The high pressure-temperature equation of state (EOS) of synthetic 13% Fe-bearing bridgmanite (Mg-silicate perovskite) is measured using powder x-ray diffraction in a laser-heated diamond anvil cell with a quasi-hydrostatic neon pressure medium. We compare these results, which are consistent with previous 300 K sound speed and compression studies, with a re-analysis of Fe-free Mg-endmember data from *Tange et al.* [2012] to determine

Sciences, University of Michigan, Ann Arbor, Michigan, USA.

[2]Division of Geological & Planetary Sciences, California Institute of Technology, Pasadena, California, USA.

[3]Hawai'i Institute of Geophysics and Planetology, University of Hawai'i, Honolulu, Hawaii, USA.

[4]GeoSoilEnviroCARS, Center for Advanced Radiation Sources, University of Chicago, Argonne National Laboratory, Argonne, Illinois, USA.

[5]Center for Advanced Radiation Sources, University of Chicago, Chicago, Illinois, USA.

the effect of iron on bridgmanite's thermoelastic properties. EOS parameters are incorporated into an ideal lattice mixing model to probe the behavior of bridgmanite at deep mantle conditions. With this model, a nearly pure bridgmanite mantle composition is shown to be inconsistent with density and compressibility profiles of the lower mantle. We also explore the buoyant stability of bridgmanite over a range of temperatures and compositions expected for Large Low Shear Velocity Provinces (LLSVPs), concluding that bridgmanite-dominated thermo-chemical piles are more likely to be passive dense layers externally supported by convection, rather than internally supported metastable domes. The metastable dome scenario is estimated to have a relative likelihood of only 4-7%, given the narrow range of compositions and temperatures consistent with seismic constraints. If buoyantly supported, such structures could not have remained stable with greater thermal contrast early in Earth's history, ruling out formation scenarios involving the concentration of radioactive elements.

1. Introduction

The Earth's lower mantle is thought to be composed of primarily aluminous $(Mg, Fe)SiO_3$ perovskite, now known as bridgmanite [*Tschauner et al.*, 2014], coexisting with $(Mg, Fe)O$ ferropericlase and $CaSiO_3$ perovskite [*Irifune*, 1994]. While the exact phase proportions depend on the assumed compositional model for the lower mantle—e.g., pyrolytic vs. chondritic—iron-bearing bridgmanite is thought to dominate, making it the most common mineral in the silicate Earth (*Kesson et al.* 1998, *Mattern et al.* 2005, *Irifune et al.* 2010), and giving it a lead role in setting the physical properties and evolution of the lower mantle.

Looking beyond average global properties, seismic studies have revealed the two largest coherent structures in the mantle, now known as large low-shear velocity provinces (LLSVPs), which contain ∼2% of the mantle's mass and occupy almost 20% of the core-mantle boundary's surface area. Located beneath Africa and the Pacific Ocean, as revealed by seismic tomography models [*Lekic et al.*, 2012], the LLSVPs are thought to potentially represent both chemically and thermally distinct structures on the core-mantle boundary [e.g., *Tackley*, 2011; *Hernlund and Houser*, 2008; *Tan and Gurnis*, 2005]. Though their location and dimensions are reasonably well characterized, the nature of LLSVPs is unknown: they may be passive piles, plume clusters, pure thermal anomalies, or metastable domes [e.g. *Davaille et al.*, 2005; *McNamara and Zhong*, 2005; *Tan and Gurnis*, 2005; *Torsvik et al.*, 2006; *Sun et al.*, 2007; *Burke et al.*, 2008; *Garnero and McNamara*, 2008; *Schuberth et al.*, 2009; *Sun et al.*, 2010; *Davies et al.*, 2012; *Steinberger and Torsvik*, 2012].

Each of these possibilities has different implications for their origin, evolution, and effect on surface geological and geochemical expressions.

LLSVPs are particularly challenging to explain, as they appear to have sharp and often steep-walled margins and stand roughly 1000 km high off the core-mantle boundary (CMB) [*Ritsema et al.*, 1998; *Ni et al.*, 2002; *Ni and Helmberger*, 2003]. The sharp seismic gradients along their edges are generally interpreted as evidence that they cannot be merely thermal anomalies, which would tend to produce diffuse margins [*Tackley*, 2011], though there is still debate in the literature on this point [*Davies et al.*, 2012]. The viewpoint of a chemically distinct pile is further bolstered by an apparent anticorrelation between shear-wave velocity anomalies and both bulk sound velocity and density anomalies within the structures relative to average mantle, contrary to the general trends of most heated material [*Ishii and Tromp*, 1999]. If they do maintain compositional differences from the average mantle, it is a challenge to understand how such structures might remain isolated for geologic time without mixing away through the process of entrainment. Since these competing hypotheses for LLSVPs rest on our understanding of material properties, characterizing the temperature- and composition-dependent equation of state of the dominant lower mantle phase, iron-bearing bridgmanite, is clearly vital to interpreting these first-order features of our planet.

Given its relevance to understanding deep-Earth phase relations, structure, and dynamics, bridgmanite has received considerable scientific attention, though exploring the relevant extreme conditions and wide range of possible chemistries represents a monumental and ongoing task. Many of the earlier x-ray diffraction studies measured bridgmanite compression and thermal expansion over a range of natural and synthetic compositions,

but experimental limitations restricted them to ambient or low pressures (< 30 GPa), largely outside bridgmanite's stability field (e.g. *Knittle et al.* 1986, *Ross and Hazen* 1989, *Mao et al.* 1991, *Wang et al.* 1994, *Funamori et al.* 1996). Later diffraction studies reached higher pressures, and used resistive or laser heating to obtain in situ high temperature measurements of thermodynamically stable bridgmanite, but were mostly performed on the pure Mg-endmember composition [e.g. *Fiquet et al.*, 1998, 2000; *Katsura et al.*, 2009; *Tange et al.*, 2012]. Recent efforts have been made to understand the compositional effects of aluminum and both ferrous and ferric iron on bridgmanite's equation of state, but have been restricted to ambient temperatures [*Daniel et al.*, 2004; *Walter et al.*, 2004; *Andrault et al.*, 2007; *Lundin et al.*, 2008; *Mao et al.*, 2011; *Catalli et al.*, 2011; *Dorfman et al.*, 2013; *Sinmyo et al.*, 2014]. First principles density functional theory calculations have also been used to predict the detailed vibrational and elastic properties of Mg-Fe bridgmanite at lower mantle pressures and temperatures [e.g. *Kiefer et al.*, 2002; *Wentzcovitch et al.*, 2004; *Metsue and Tsuchiya*, 2012]. *Glazyrin et al.* [2014] recently investigated the compression and high pressure thermal expansion of aluminum- and ferric iron-bearing bridgmanite, giving insights into the properties of subducted oceanic crust. Raman and Brillouin spectroscopy as well as ultrasonic interferometry have also been used to help constrain the Mg-endmember's vibrational properties and sound velocities [e.g. *Gillet et al.*, 1996; *Chopelas*, 1996; *Sinogeikin et al.*, 2004; *Li and Zhang*, 2005; *Chantel et al.*, 2012; *Murakami et al.*, 2012].

While important to our understanding of the deep Earth, complex compositional studies are challenging to clearly interpret, and thus we must also turn to simpler systems where we can develop a well-characterized understanding of our observations. With this

motivation, we determine the temperature-dependent equation of state for polycrystalline perovskite-structured $(Mg_{0.87}Fe_{0.13})SiO_3$ (synthetic ferrous bridgmanite), using a novel Bayesian fitting procedure that properly accounts for all major measurement error sources (see **pvt-tool**, *http://github.com/aswolf/pvt-tool*). Though non-hydrostatic stress states have been shown to potentially alter a mineral's compression behavior [e.g., *Fei*, 1999; *Takemura*, 2007; *You Shu-Jie and Chang-Qing*, 2009; *Iizuka et al.*, 2010], most diamond anvil cell studies have used strongly non-hydrostatic pressure media, including bulk loading without a medium, NaCl, and Ar; to address this problem, we conduct these compression experiments in a quasi-hydrostatic neon pressure medium. This sample was probed with x-rays under a wide range of conditions between 30 and ∼130 GPa and room temperature up to ∼2500 K, all of which were entirely within the bridgmanite stability field. Synchrotron Mössbauer spectroscopy measurements were also made after the highest P-T diffraction observation, showing that iron within the sample remains in the high-spin ferrous valence state even up to ∼120 GPa (at 300 K), confirming the sample's integrity against phase separation or chemical diffusion throughout the experiment. These results are then compared with a careful reanalysis of the Fe-free $MgSiO_3$ bridgmanite data from *Tange et al.* [2012] to assess the effect of ferrous iron on bridgmanite's high-temperature compression behavior.

The resulting equation of state models for Fe-bearing and Fe-free bridgmanite are combined to assess both low- and high-pressure thermoelastic properties. We demonstrate that our equation of state results are fully consistent with previous measurements when the zero-pressure volume parameter V_0 is fixed to the anomalously large ambient volumes characteristic of thermodynamically metastable bridgmanite. Combining the two equa-

tions of state using an ideal lattice mixing model, we obtain thermoelastic properties for a wide range of compositions up to 25% ferrous iron. By calculating self-consistent mantle adiabats, combined with a representative core-mantle thermal boundary layer, we demonstrate that bridgmanite alone is incapable of matching the densities and compressibilities of the bulk mantle (PREM), ruling out the possibility of a bridgmanite-only lower mantle chemistry.

These findings are finally used to explore bridgmanite's potential role in the behavior of deep-Earth structures. We perform a buoyant stability analysis to test the possibility of compositionally distinct bridgmanite-dominated structures at the base of the lower mantle as a model for the seismically observed LLSVPs. Through this investigation, we show that the passive chemical pile hypothesis for LLSVPs is favored over the metastable dome hypothesis based on the range of temperature-composition values that are supportive of each scenario.

2. Experimental Methods

2.1. Sample Preparation and Data Collection

The polycrystalline bridgmanite sample was made from synthetic orthopyroxene-structured $(Mg_{0.87}{}^{57}Fe_{0.13})SiO_3$ starting material. This composition was verified using micro-probe analysis, and initial synchrotron Mössbauer spectroscopy showed it to contain undetectable levels of ferric iron, constraining it to less than 3% Fe^{3+}—see Section 2.3 for details [*Jackson et al.*, 2009; *Zhang et al.*, 2011]. The sample was loaded into a symmetric diamond anvil cell using a pre-indented Re gasket with beveled 250 micron culets. The sample was also loaded with synthetic ruby spheres for offline pressure determination using the ruby fluorescence method [e.g., *Jacobsen et al.*, 2008; *Silvera et al.*,

2007]. The cell was filled with a Ne pressure medium using the GSECARS gas-loading system at the Advanced Photon Source of Argonne National Laboratory [*Rivers et al.*, 2008] and then pressurized to ∼30 GPa where it was laser annealed within the stability field of bridgmanite.

High temperature powder x-ray diffraction (XRD) experiments were conducted at the 13-ID-D beamline (GeoSoilEnviroCars) at the Advanced Photon Source, Argonne National Laboratory. Using an incident x-ray wavelength of $\lambda = 0.3344$ $\mathring{A}$ and focus spot size of better than 4 μm x 4 μm, angle-dispersive X-ray diffraction patterns were recorded onto a MAR165 CCD detector. CeO_2 was used to calibrate the sample to detector distance at 1 bar. Diffraction patterns were taken in roughly 2 to 4 GPa steps between about 33 and 120 GPa (non-heated pressure range). The pressure for each measurement was determined using the Ne pressure medium as the primary pressure marker [*Dewaele et al.*, 2008], detailed in Section 3.1, together with the offline ruby fluorescence measurements for secondary verification. High temperatures were achieved in-situ using double-sided laser heating with 1.064 μm Yb fiber lasers with 'flat top' intensity profiles [*Prakapenka et al.*, 2008], enabling uniform laser heating of the complete sample area (20-25 microns) while minimizing temperature gradients and suppressing possible thermally induced iron partitioning. Laser heating was carried out in roughly 5 to 10 GPa steps, where the laser power was gradually increased over a series of stages to measure sample behavior ranging between about 1600 K and 2500 K. These temperatures were determined spectro-radiometrically [e.g. *Heinz and Jeanloz*, 1987; *Shen et al.*, 2001] using the gray-body approximation over the 600-800 nm range of thermal emission.

In addition to these experiments, we also rely upon data for the Fe-free endmember $MgSiO_3$ bridgmanite, reported by *Tange et al.* [2012]. While there are numerous studies of this composition (see Introduction), we chose this dataset for its similar P-T range, usage of an up-to-date thermal pressure marker, and favorably low uncertainties for the sintered-diamond multi-anvil data points. These characteristics are discussed in more detail in Section 3.1. By following an identical procedure for analyzing both our new Fe-bearing data and the iron-free data from *Tange et al.* [2012], we can make confident comparisons of the two equations of state knowing that differences in model fitting and error analysis have been removed.

2.2. High P-T Sample Characterization

The sample's high pressure phase assemblage is readily determined from the processed powder diffraction images. The raw diffraction images are converted into background-subtracted one-dimensional patterns using a suite of routines written in MATLAB (see Appendix A for details on the data reduction pipeline). Figure 1 displays a set of representative patterns, together with an interpolated compression map at 300 K, showing the basic compression trends of each diffraction line at room temperature. We also overplot the fitted line positions for each phase, showing that dozens of bridgmanite peaks are visible in the pattern along with peaks from other materials in the sample chamber, including the high-intensity peaks from neon that are used as in situ pressure markers as described in Section 3.1.

A recent study by *Zhang et al.* [2014] found that under specific pressure-temperature conditions, iron-bearing bridgmanite was observed to undergo ex-solution, disassociating into two different phases: an iron-free bridgmanite and an iron-rich distorted hexagonal

phase (dubbed the H-phase). *Zhang et al.* [2014] report finding the H-phase, evident by its characteristic diffraction peaks at 2.4 and 2.55 $\mathring{A}$, only when the silicate sample was brought up to very high pressure without annealing within the bridgmanite stability field, corresponding to cold compression from ambient conditions up to about 90 GPa, and then laser heated to temperatures above about 2000 K. Though we did not follow this particular P-T pathway, we nevertheless search our diffraction data, but fail to find any evidence of the H-phase, as indicated by the red-boxed zoomed regions of Figure 1. While there does appear to be a slight intensity increase close to 0.416 $\mathring{A}^{-1}$ (2.4 $\mathring{A}$), the amplitude is well within the noise of the measurements and maintains constant position over the entire pressure range, indicating that it cannot represent a diffraction line for a phase undergoing compression. Though these data cannot rule out the existence of the H-phase for Fe-bearing bridgmanite systems, neither do they lend support.

2.3. Inferring Iron's Valence and Spin State using Synchrotron Mössbauer Spectroscopy

Synchrotron Mössbauer spectroscopy (SMS) is a well-established tool for characterizing the local electronic environment of iron atoms, enabling exploration of valence, spin state, and atomic site distortions [e.g. *Sturhahn and Jackson*, 2007]. To constrain the valence and spin state of iron in our bridgmanite sample, SMS experiments were performed at beamline 3-ID-B of the Advanced Photon Source [e.g. *Sturhahn*, 2004] immediately following the high P-T x-ray diffraction experiments. After the sample had achieved the highest P-T conditions, it was quenched to 300 K and P_{ne} = 117 GPa, and then brought to Sector 3 for the SMS measurements. The x-rays at 3-ID-B were prepared with a bandwidth of 1 meV using a multiple crystal Bragg monochromator [*Toellner*, 2000] and a focus

spot-size of about 10 μm x 11 μm (which effectively probes the entire previously heated region of the bridgmanite sample given the extended tails of the x-ray beam at 3-ID-B). The storage ring was operated in low emittance top-up mode with 24 bunches that were separated by 153 ns. Accounting for detector-related effects, we were able to observe nuclear resonant scattering in a time window of 16 to 127 ns following excitation. The quadrupole splitting, broadening, and weight fractions of the iron sites are determined by analysis of the SMS time spectrum (see Figure 2), which was obtained with a 3 hour collection time. Further constraints on the hyperfine parameters, such as the isomer shift and the physical thickness of the sample, are obtained by collecting an additional time spectrum with an added natural stainless steel foil (with a physical thickness of 3 μm) in the x-ray beam path [*Alp et al.*, 1995]. The measured SMS spectra were evaluated using the CONUSS software [*Sturhahn*, 2000].

The SMS time-spectrum collected without the stainless steel foil, shown in Figure 2, which is clearly dominated by a single oscillatory frequency. The corresponding power spectrum is shown in the inset figure, which confirms a primary frequency induced by a quadrupole splitting of $\sim$4.4 mm/s, but also reveals a broad feature underlying this sharp peak. As shown by the solid red line representing the best-fit model, the data can be well represented (reduced $\chi^2 \approx 1.5$) with about 50% texture and two sites, distinguishable only by the broadening of the electric field gradient (or full width at half-maximum of the quadrupole splitting, FWHM). Thus, each iron-site can be characterized by the following hyperfine parameters: quadrupole splitting (QS) of $4.38 \pm .01$ mm/s and an isomer shift (IS) of 0.98 ± 0.02 mm/s (where the isomer shift value is reported relative to α-Fe). The dominant site ($77 \pm 3\%$) is relatively sharp with a FWHM of $0.14 \pm .01$ mm/s and the

broadened site can be described with a FWHM value of $1.20 \pm .05$ mm/s, which is likely due to the combined effect of atomic site distortions and the pressure gradient sampled by the x-ray profile. This set of hyperfine fields is indicative of high-spin ferrous iron in the bipolar-prismatic site (the A site) in the Pbnm-perovskite (bridgmanite) structure [e.g. *Jackson et al.*, 2005; *Li et al.*, 2006; *McCammon et al.*, 2008; *Bengtson et al.*, 2009; *Jackson et al.*, 2009; *Catalli et al.*, 2010a, b; *Hsu et al.*, 2010a, b, 2011].

To verify the robustness of this model, we also fit numerous comparison models. First it should be noted that a single site model does not provide an adequate fit to the data, as evidenced by the need to match the broad underlying feature seen in the power spectrum. Likewise, a 3-site model that includes separate sites with QS values of 3.2 mm/s, 4.4 mm/s, and 5.7 mm/s, also provides a poor match to the data, despite the introduction of many more free parameters. Moreover, that model's third site has an unphysically large QS value for bridgmanite [*McCammon et al.*, 2008], indicating that the apparent satellite peaks in the power spectrum actually represent a broadened distribution of field gradients ($\sim$1.2 mm/s) centered on a quadrupole splitting of $\sim$4.4 mm/s.

We also explore alternate models that include additional sites with low quadrupole splitting. The well-separated feature found in the power spectrum at a QS of $\sim$0.7 mm/s is potentially indicative of a small degree of high-spin ferric iron. Using the Monte Carlo algorithm in CONUSS, a second plausible model is found to fit the data almost as well (reduced $\chi^2 \approx 1.9$), with the addition of four more free parameters (QS, FWHM, IS, and weight fraction) describing a third low QS Fe-site. Though this second model, shown as the red-dashed line in Figure 2, provides an adequate description of the data, it is not statistically favored due to its higher complexity and somewhat poorer fit quality. The hyperfine

parameters of its two high QS sites agree with those of the primary model described above to within uncertainties, and the third site has QS=0.62(1) mm/s, FWHM=0.70(8) mm/s, and IS=0.18(1) mm/s. These values are consistent with high-spin ferric iron [*McCammon et al.*, 2008; *Hsu et al.*, 2011], though they represent only 5% of the total iron present, thus providing an upper limit for the ferric iron content. We also explored the possibility of a low QS Fe^{2+} site (QS$\sim$2.4 mm/s), which is suggested to be present in bridgmanite at pressure below about 30 GPa [*Hsu et al.*, 2010b], however the data do not support this model, as the fitting procedure reverts this additional ferrous site to a QS of 4.21(1) mm/s, similar to previous models.

Taken together, these analyses provide strong constraints on the state of iron within the entire bridgmanite sample, indicating that it has remained in-place and almost entirely in the 2+ valence state. If iron diffusion occurred such that $(Mg, Fe)O$ and SiO_2 exsolved, one would expect to find a low spin (LS) ferropericlase feature in our spectrum. However, the spectrum cannot be fit with a site similar to that of LS $(Mg, Fe)O$, which has a QS=0, IS of around 0.3 to 0.8 mm/s, and is typically broad. Previous investigations of $(Mg_{0.88}Fe_{0.12})SiO_3$ bridgmanite reported significant broadening of the high quadrupole site [*McCammon et al.*, 2008] in both conventional and time-domain Mössbauer spectroscopy measurements, in support of our primary model. In addition to the broadened ferrous-like site, these measurements also report a few weight percent of a relatively constant low QS site (QS$\sim$0.5 to 1.0 mm/s and IS$\sim$0.4 mm/s) at 300 K throughout the compression study up to 110 GPa (annealed up to $\sim$1000 K), interpreted as high spin Fe^{3+} [*McCammon et al.*, 2008]. However, if Fe^{3+} is indeed present, one would expect Fe metal to also be present [*Frost et al.*, 2004], but a final model exploring this hypothesis was non-convergent,

ruling out the presence of detectable metallic iron. We can therefore surmise that there is no clear evidence for iron diffusion in response to laser-heating, as nearly all the iron appears to remain within bridgmanite in its original high-spin ferrous state.

3. Analysis

In order to obtain volume estimates for determining bridgmanite's equation of state, we utilize peak-fitting to extract unitcell dimensions from our 1D diffraction patterns. While more time-consuming than the whole pattern refinement method [e.g. *Toby*, 2001], individual peak-fitting is useful for lower symmetry phases like bridgmanite, which contain a large number of strongly overlapping peaks which also share diffraction space with other phases present in the sample chamber (see the high inverse-d spacing region of Figure 1). By limiting the potentially biasing influence of unidentified sample peaks as well as stray peaks from unknown phases, the peak-fitting approach can yield more robust volume estimates. We use a custom peak-fitting code written in MATLAB that combines automated minimization with user-driven commands, inferring the sample peak positions by fitting pseudo-Voigt peak profiles to the set of observed and identified diffraction peaks. The set of resulting peak positions are shown as color-coded ticks and crosses in Figure 1. From this list of sample peak positions, including between 10 and 25 identified bridgmanite peaks per diffraction pattern, we obtain estimates of volumes (given in Table 1) and unitcell dimensions using a robust Bayesian peak-list fitting routine (details found in Appendix B).

3.1. P-T Conditions

In situ temperature estimates during laser-heating are obtained from measurements of the thermal emission of the sample. The laser heating system at the Sector 13-ID-D beamline of GSECARS is equipped with a set of optics that simultaneously focus a laser-heating spot on the sample, while carrying the thermally radiated light from the sample back to two independently calibrated spectrometers [*Prakapenka et al.*, 2008]. The sample's thermal radiation spectrum is fit at the beamline assuming a gray-body spectrum [e.g. *Heinz and Jeanloz*, 1987; *Shen et al.*, 2001], enabling estimation of the temperature for both upstream and downstream sides of the sample, with estimated experimental uncertainties of ∼100 K.

In our experiments, we rely primarily on the diffraction peaks of the quasi-hydrostatic neon pressure medium to determine in situ pressures. Note that we use the high-temperature thermally-expanded neon in contact with the sample to determine pressures (rather than the colder denser neon in contact with the diamond surfaces). While Au was also placed inside the sample chamber, the majority of the powder diffraction patterns show weak or absent Au peaks. In contrast, the diffraction lines from neon give the most intense reflections in every pattern. When present, Au peaks allowed confirmation of the pressures inferred from neon in the unheated spectra.

Using the same peak-fitting procedure described above for bridgmanite, we retrieve peak positions for both the neon 111 and 200 lines. Despite the favorable properties of neon for reducing deviatoric stresses, they often persist at high pressures, inducing differences in apparent unitcell volumes from each diffraction line [see for example *Dorfman et al.*, 2012]. We therefore use the primary 111 peak in order to determine the neon unit cell volumes (see Table 1), which due to its high intensity and position within the diffraction

pattern is relatively free from the biasing effects of overlapping sample peaks. Neon volumes are converted into pressure estimates using the well-determined equation of state reported in *Dewaele et al.* [2008], which provides a carefully constrained Mie-Grüneisen-Debye equation of state using high-cadence room-temperature compression data up to 200 GPa and precise resistive-heating high-temperature measurements between 300 K and 1000 K. A detailed discussion of pressure uncertainties and error propagation is given in Section 3.4.

In order to have confidence in the resulting Fe-bearing bridgmanite equation of state, we must pay careful attention to the basis of the secondary Ne-pressure scale, which rests upon the calibration of the SrB_4O_7:Sm^{2+} fluorescence pressure scale [*Datchi et al.*, 1997, 2007], that is in turn tied to the *Holzapfel et al.* [2005] ruby pressure-scale. Like ruby, SrB_4O_7:Sm^{2+} exhibits a pressure-dependent fluorescence line shift, but is better suited to high temperature experiments since the shift is nearly independent of temperature. Additionally, it shows little dependence on deviatoric stress state and remains high in intensity to very high pressure. *Datchi et al.* [2007] showed that by calibrating the scale against Holzapfel's (2005) ruby scale, the SrB_4O_7:Sm^{2+} scale accurately recovers the ab-initio predictions for the equations of state of both diamond and cubic boron nitride. We therefore have confidence that Dewaele's [2008] neon pressure scale provides the best-available neon-based estimate of pressure, which should also correspond closely to the true pressure conditions.

To assess the affect of ferrous iron, we compare the behavior of our 13% Fe-bearing sample to that of Fe-free bridgmanite, based on the data of *Tange et al.* [2012]. While those experiments did not use a neon pressure medium, they carefully utilized extensive thermal

relaxation in order to minimize non-hydrostatic stresses. The *Tange et al.* [2012] pressure estimates rely on the MgO pressure scale of *Tange et al.* [2009a], which makes use of a so-called Scale-Free Unified Analysis approach, combining measurements of quantities that do not rely on any pressure scale—including thermal expansion, adiabatic bulk modulus, and shock Hugoniot data. We therefore consider the *Tange et al.* [2009a] MgO pressure scale to be of excellent quality, providing a good estimate of pressure that closely reflects the absolute stress conditions.

3.2. The Mie-Grüneisen-Debye Equation of State

Following after previous investigators, we use the Mie-Grüneisen-Debye model to represent the equation of state of bridgmanite over a wide range of temperatures and pressures. This description employs the thermal pressure approximation, which divides the free energy into *cold* and *thermal* components, leading to separate contributions to the pressure. For convenience, the *cold* contribution to the pressure is often defined with reference to ambient temperature conditions, $T_0 = 300K$, rather than absolute zero, yielding the total pressure expression:

$$P(V,T) = P_{\rm ref}(V) + P_{th}(V,T) - P_{th}(V,300{\rm K}) \quad (1)$$

where $P_{\rm ref}$ is the *cold* contribution to the total pressure given by the 300 K reference isotherm, and P_{th} is an expression for the *thermal* contribution, both described below.

At ambient temperature conditions (in the absence of phase transitions), most solid materials are well described by a Vinet equation of state [*Vinet et al.*, 1989]. *Cohen et al.* [2000] showed that the Vinet equation of state is generally favored over the more commonly used third-order Birch-Murnaghan, yielding more accurate extrapolation behavior over

large compression ranges. The Vinet equation is given by:

$$P_{\mathrm{ref}}(x) = 3K_{0T}(1-x)x^{-2}\exp\left[\nu(1-x)\right]$$
$$\text{where} \quad x = (V/V_0)^{\frac{1}{3}} \quad \text{and} \quad \nu = \frac{3}{2}(K'_{0T}-1) \tag{2}$$

where x is the average axial strain, V_0 is the zero-pressure volume, K_{0T} is the zero-pressure isothermal bulk modulus, and K'_{0T} is its derivative ($K' \equiv \partial K/\partial P$).

The thermal pressure component is evaluated using the Debye crystal model to approximate the energetic contribution of thermal vibrations in a crystalline solid. This simplified vibrational model is derived for monatomic solids, but has been shown to approximately hold true for a limited class of crystals—marked by a sudden drop-off in their phonon density of state curves at a characteristic cut-off frequency—which includes bridgmanite [*Anderson*, 1998]. The Mie-Grüneisen-Debye expression for the thermal pressure is:

$$P_{th}(V,T) = \frac{\gamma}{V}E_{\mathrm{th}} = \frac{\gamma}{V}\left[C_V^{\max}TD\left(\frac{\Theta}{T}\right)\right] \tag{3}$$

where γ is the thermodynamic Grüneisen parameter and E_{th} is the thermal energy given by the Debye model. The Debye energy depends on the Dulong-Petit high-temperature limit for the volumetric heat capacity $C_V^{\max} = 3k_B N_{\mathrm{cell}}$, and the Debye temperature Θ, which sets the energy-scale for the approximate phonon density of states representation. The function $D(x)$ is the Debye integral, which represents how the vibrational heat capacity varies with temperature:

$$D(x) = \frac{3}{x^3}\int_0^x \frac{y^3 dy}{e^y - 1} \tag{4}$$

where the integral, which must be evaluated numerically, is a function of $x = \Theta/T$, asymptotically approaching the high temperature limit of 1 as $x \to 0$.

The Grüneisen parameter is a particularly important thermodynamic quantity, that defines the temperature path along an adiabatic compression curve, $\gamma \equiv -(\partial \log T/\partial \log V)_S$.

To complete the equation of state parameterization, we use the common power-law expression for the Grüneisen parameter:

$$\gamma(V) = \gamma_0(V/V_0)^q \tag{5}$$

where γ is independent of temperature (as required by the Mie-Grüneisen approximation) with a reference value of γ_0 at V_0 and a compression sensitivity described by the power-law exponent q. The corresponding compression dependence of the Debye temperature is:

$$\Theta(V) = \Theta_0 \exp[-(\gamma - \gamma_0)/q] \tag{6}$$

where Θ_0 is the reference Debye temperature at V_0. Over the pressure-temperature range of this study, we find this common parametrization is fully sufficient to represent the data.

3.3. Inferring the Equation of State Parameters from PVT Data

Using the model described above, the high P-T datasets for the 13% Fe-bearing bridgmanite of this study and the Fe-free bridgmanite of *Tange et al.* [2012] (Tables 1 & 2) are fit to obtain their equation of state parameters (Table 3). To accomplish this task, we have written a custom MATLAB code called **pvt-tool** (publicly available at *http://github.com/aswolf/pvt-tool*), that is designed to enable fitting of high temperature compression data while properly accounting for prior information and correlated uncertainties in the data. This is achieved in two stages: first the *cold* parameters V_0, K_{0T}, and K'_{0T} are estimated using ambient temperature data and then the *thermal* parameters Θ_0, γ_0 and q are inferred from the heated data. According to standard Bayesian practice, we use priors to capture outside knowledge about the likely range of values for each parameter. Past studies have shown that ambient bridgmanite volumes display a relative scatter that far exceeds measurement uncertainties (even at fixed composition), implying

that there is some unmodeled source of sample-to-sample variability. This behavior is shown in Figure 3, which combines data compiled by *Kudoh et al.* [1990] with a number of more recent studies to show both the compositional trend and high variability in ambient pressure volumes for bridgmanite. This variability may stem from the fact that at 0 GPa, bridgmanite is far outside its thermodynamic stability range, potentially leading to inconsistent decompression behavior. Despite this complication, we can estimate the linear dependence of V_0 on Fe-composition along with its scatter, as shown by the solid and dashed lines in the figure, providing useful prior estimates of the zero-pressure volume for 13% Fe-bearing and Fe-free bridgmanite of 163.2 ± 0.2 and 162.5 ± 0.2 $\mathring{A}^3$, respectively.

For the other *cold* parameters K_{0T} and K'_{0T}, we forgo informative priors since both datasets easily constrain these variables. For the *thermal* parameters, we impose weakly informative priors of $\gamma_0 = 1 \pm 1$ and $q = 1 \pm 1$, indicating their order of magnitude and tendency toward positive values. Finally, we do not attempt to directly determine the value of the reference Debye temperature Θ_0 for both datasets, as it is not well-constrained for the 13% Fe-bearing sample. (This is because all the laser-heated measurements had temperatures well above Θ_0, thus approaching the Dulong-Petit high-temperature limit, which is independent of Θ.) Instead, we first determine the best-fit value of the reference Debye temperature for the Fe-free dataset, assuming a weakly informed (wide) prior of $\Theta_0 = 1070 \pm 150$ K, based on the approximate relation between wave velocities and the Debye temperature [*Anderson*, 1998] using measured zero-pressure velocities for Fe-free bridgmanite from Brillouin spectroscopy [*Sinogeikin et al.*, 2004]. This initial fit yields an optimal value of $\Theta_0 = 991 \pm 77$ K and shows that the remaining parameters are all relatively uncorrelated with the Debye temperature, where the largest correlation

coefficient (between Θ_0 and γ_0) was only +0.60. To simplify the analysis and reporting, we proceed by fixing the value of the Debye temperature to $\Theta_0 = 1000$ K, fully consistent with this best fit, and assume that it remains independent of composition (sensitivity to this assumption discussed later in Section 4.2).

The final best-fit parameter values are presented in Table 3 for both Fe-bearing and Fe-free bridgmanite samples, and the corresponding equation of state models are visualized together with the data in Figure 4. The upper and lower panels show the data for the 13% Fe and Fe-free datasets, respectively, color-coded by temperature, along with the 300 K-reduced pressure isothermal data as open circles (calculated by subtracting off the thermal pressure contribution for each data point). These isotherm-reduced data compare well with the 300 K model isotherms, shown as solid blue lines.

The confidence bounds on these model parameters are determined from the covariance matrix, using the standard approach for weighted least-squares modeling. To verify the results from **pvt-tool** (*http://github.com/aswolf/pvt-tool*), we perform the same fit to the error-adjusted dataset in Table 3 with the tested open-source software **MINUTI** (*http://www.nrixs.com*), obtaining results that agree well within mutual uncertainties with nearly identical correlation matrices.

3.4. Estimating realistic measurement uncertainties

Accurate measurement errors play a crucial role in determining the equation of state parameter values and uncertainties discussed above. This is because data errors provide a weighting scheme for the relative importance of each measurement, while also setting the overall scale for the parameter uncertainties. Further complication for the fitting procedure arises from the fact that errors in measured quantities appear on both dependent

and independent variables P, T, and V. This situation is easily remedied using standard error propagation methods to determine the effective error in pressure misfit, ΔP, given by:

$$\Delta P = P_{\mathrm{mrk}}(T, V_{\mathrm{mrk}}) - P_{\mathrm{smp}}(T, V_{\mathrm{smp}}) \tag{7}$$

where "mrk" and "smp" refer to the corresponding values for the pressure marker and sample phases (i.e. neon/MgO and bridgmanite). By focusing on the data vectors $(V_{\mathrm{mrk}}, V_{\mathrm{smp}}, T)$ rather than the more familiar (P, V_{smp}, T), we dramatically simplify the error propagation procedure, since uncertainties on the directly measured quantities are independent, and therefore add in quadrature:

$$\begin{aligned}\sigma^2_{\Delta P} \approx &\left(\frac{\partial P_{\mathrm{mrk}}}{\partial T} - \frac{\partial P_{\mathrm{smp}}}{\partial T}\right)^2 \sigma^{*2}_T + \\ &\left(\frac{\partial P_{\mathrm{mrk}}}{\partial V_{\mathrm{mrk}}}\right)^2 \sigma^{*2}_{V_{\mathrm{mrk}}} + \left(\frac{\partial P_{\mathrm{smp}}}{\partial V_{\mathrm{smp}}}\right)^2 \sigma^{*2}_{V_{\mathrm{smp}}}\end{aligned} \tag{8}$$

The σ^* terms above represent the adjusted measurement uncertainties for each quantity (more details below), and derivatives are evaluated locally. With this expression, we determine how much uncertainties in sample volume, marker volume, and temperature each contribute to the total effective pressure uncertainty. To get reasonable values for the marker volume errors in our experiment, we assume that the fractional volume uncertainty of neon matches the average for the bridgmanite sample, since both result from peak position errors. When applied to the two datasets considered in this study, we find that the marker and sample volume errors both contribute meaningfully to the overall pressure uncertainty, while temperature errors contribute negligibly, as discussed in detail below.

The total propagated uncertainties are then incorporated into a *cost function* which expresses the goodness-of-fit of a set of model parameters, often written in terms of χ^2

with an additional penalty term that incorporates prior information:

$$\mathcal{C} = \sum_{i}^{\text{obs}} \frac{1}{2} \left(\frac{\Delta P_i(\boldsymbol{\phi})}{\sigma_{\Delta P_i}} \right)^2 + \sum_{j}^{\text{params}} \frac{1}{2} \left(\frac{\phi_j - \bar{\phi}_j}{\sigma_{\phi j}} \right)^2 \tag{9}$$

where the model residuals ΔP_i are a function of the model parameters $\boldsymbol{\phi}$, and the priors are given by $\bar{\phi}_j \pm \sigma_{\phi j}$ for the j^{th} model parameter. According to the standard least-squares approach, minimizing the cost-function value yields the best-fit equation of state parameters. Additionally, the covariance matrix, which expresses how uncertainties in the different model parameters are correlated with one another, is determined from the curvature of the cost-function, $\boldsymbol{\Sigma} \approx (\boldsymbol{\nabla^2 \mathcal{C}})^{-1}$, in the local region around the best fit.

Given the important role that parameter uncertainties play in comparing equations of state across different studies or materials, total propagated error bars must accurately reflect pressure misfits. We therefore introduce an additional error modeling procedure, implemented in **pvt-tool**, which adjusts the reported error bars by an empirical corrective percentage, in order to obtain final model residuals that are consistent with the total propagated errors:

$$\begin{gathered} \sigma^*_{V_{\text{mrk}}} = \sigma_{V_{\text{mrk}}} \exp\{\delta_V\} \quad , \quad \sigma^*_{V_{\text{smp}}} = \sigma_{V_{\text{smp}}} \exp\{\delta_V\} \\ \sigma^*_T = \sigma_T \exp\{\delta_T\} \end{gathered} \tag{10}$$

where the adjustment is applied separately to the volume and temperature terms using $\exp\{\delta_V\}$ and $\exp\{\delta_T\}$ as weighting factors, inflating or deflating these error sources as appropriate. Since measurement uncertainty systematics differ depending on data source, we introduce independent error-model parameters for each data source (such as sintered-diamond multi anvil and diamond anvil cell experiments), as indicated by the measurement group IDs in Tables 1 and 2.

The parameter values for the equation of state model and the error model must be refined iteratively, since the equation of state model relies on the propagated uncertainties for each measurement, which themselves depend on the best-fit residuals. Parameter estimates are thus obtained by first fitting the equation of state without adjustments to reported error bars by minimizing Equation (9). Next the error adjustment parameters are fit given these initial residuals, using the following error-model cost function

$$\mathcal{C}_{\rm err} = \sum_i^{\rm obs} \frac{1}{2} \left(\frac{\Delta P_i}{\sigma_{\Delta P_i}(\delta V, \delta T)} \right)^2 + \sum_i^{\rm obs} \log_e \sigma_{\Delta P_i}(\delta V, \delta T) \quad (11)$$

where the model residuals are held fixed and only the uncertainty adjustment parameters δV and δT are allowed to vary, expressing how the size of the error bar $\sigma_{\Delta P}$ affects the relative likelihood of a set of observations. In reality, this cost function is considered separately for each independent measurement group, each with their own values of δV and δT to be optimized (see group IDs in Tables 1 and 2). By minimizing Equation (11) with respect to δV and δT individually for each measurement group, we can infer the most probable uncertainty adjustment terms for each data source. The equation of state parameters are then finalized given the updated measurement uncertainties (further iteration yields negligible changes). The favorable results of this error adjustment scheme are demonstrated in the insets of the upper and lower panels in Figure 4, which show histograms of the normalized residuals to the best-fit. The histograms are broken into ambient temperature measurements in blue and heated measurements in red, yielding the total bin counts in black. The results of this error modeling procedure are that volume error bars are adjusted up or down by up as much as $\sim$50%, as demanded by the model residuals, while temperature error bars receive negligible adjustment.

The most counterintuitive outcome of this careful error analysis is that *random temperature errors have almost zero impact on the analysis* due to a near-perfect cancellation of temperature derivatives. This can be seen in the temperature scale factor in Equation (8), which depends on the difference in thermal pressures between sample and pressure marker. Even for materials with very different thermal properties, such as bridgmanite and compressed neon, thermal pressure differences are rather small, leading to propagated temperature errors of less than 0.03 GPa.

While this analysis indicates that temperature errors do not play a *direct* role in the modeling of these data, it does not mean that experimental heating does not increase uncertainties. Inherent in the construction of Equation (8) is the assumption that the sample and the marker materials are both at the same temperature and that the sample chamber is free of thermal gradients. Though much effort has been taken to minimize these sources of error, it is impossible to eliminate thermal gradients in the presence of micro-focused x-ray diffraction and laser-heating. The errors in pressure therefore stem, not from random error propagation, but rather from non-ideal experimental conditions. The inevitable presence of thermal gradients within the diamond anvil cell leads to pressure gradients that drive flows to relax stresses. These relaxations induce spatial variations in unit cell volumes that contribute to volume uncertainties. To account for these thermally-induced uncertainties, we adopt the practical approach of placing in situ laser-heated measurements into a separate measurement group from ambient measurements (see Tables 1 & 2). This allows the error model to empirically determine the additional errors induced by thermal gradients without needing an explicit physical model. The final adjusted uncertainties, and corresponding propagated uncertainties in pressure mis-

fit are shown in Tables 1 and 2 and were used to obtain our parameter estimates and uncertainties reported in Table 3.

4. Discussion

Given the models for Fe-free and 13% Fe-bearing bridgmanite, we now take a deeper look into the effect of ferrous Fe on bridgmanite's equation of state. Our results are compared with previous studies and the covariance estimates are used to assess our degree of confidence in these apparent differences under a range of pressure-temperature conditions. Finally, we incorporate the equation of state determinations into an ideal mixing framework in order to evaluate the plausibility of different bridgmanite-rich compositional models for deep mantle structures.

4.1. Compression Evolution of the Perovskite Crystal Structure

As investigated by other authors, we can compare the evolution of the crystal axial ratios with compression. Past work [*Lundin et al.*, 2008; *Dorfman et al.*, 2013] has found that the addition of iron causes a noticeable change in the normalized axial ratios, which are generally observed to grow roughly linearly with pressure. The normalized unitcell parameters are defined as: $a^* = a(V/\sqrt{2})^{-1/3}$, $b^* = b(V/\sqrt{2})^{-1/3}$, and $c^* = c(2V)^{-1/3}$ [*Andrault et al.*, 2007], constructed to yield values of one for an ideal cubic perovskite crystal structure and deviate progressively with increasing distortion. To track compression effects on the unitcell geometry, we use the linear compression ratio $(V/V_0)^{-1/3}$ in place of pressure, since it provides an intuitive purely geometric indicator of the degree of compression that is independent of temperature, thereby removing thermal pressure effects.

The compression evolution of the normalized axial ratios is shown for both bridgmanite samples in the upper panel of Figure 5. The Fe-bearing sample is depicted with red crosses and the Fe-free sample from *Tange et al.* [2012] with black circles. These axial ratios can be converted into an estimate of the tilt angle of the corner-sharing silica octahedra comprising the backbone of the perovskite structure. From *O'Keeffe et al.* [1979], we can calculate the octahedral tilt angle as a function of the unit cell parameters:

$$\psi = \cos^{-1}\left(\frac{\sqrt{2}a^2}{cb}\right) = \cos^{-1}\left(\frac{1}{(c/a)^*(b/a)^*}\right) \quad (12)$$

where $(c/a)^*$ and $(b/a)^*$ are the normalized axial ratios. In the lower panel of Figure 5, we show the nearly linear evolution of the octahedral tilt angle with compression, demonstrating how the gradual distortion of the perovskite unitcell is accommodated by the progressive tilting of these octahedra. It is clear from this figure that the compression trends for Fe-bearing bridgmanite are offset from the Fe-free trend, as found by previous authors [*Lundin et al.*, 2008; *Dorfman et al.*, 2012], where the addition of 13% Fe tends to reduce the octahedral tilt angles by about a half-degree. We can also see the hint of a change in slope for the axial tilt trend apparent at the low pressure end (linear compression ratio of 1.04), corresponding to ambient pressures below ∼40 GPa. Since nearly all our data are above this pressure, this observation is fairly tentative, but it is consistent with the ambient temperature observations of a change in tetragonal shear strain evolution around ∼40 GPa for 4% Fe-bearing bridgmanite [*Ballaran et al.*, 2012].

4.2. Equation of State Comparison and Uncertainties

Teasing out the effects of ferrous iron on the equation of state of bridgmanite requires careful inter-comparison of our parameter confidence regions for the Fe-free and Fe-bearing

samples, as well as with previously published results. The correlation matrices in Table 4 show strong correlations for the *cold* parameters (K_{0T}, K'_{0T}) and *thermal* parameters (γ_0, q), reflecting the general trade-off between slope and curvature in matching the observed sample volumes across wide ranges of pressure and temperature. Correlations between the remaining parameters are all fairly small with the exception of (V_0, K_{0T}), which reveals how poorly constrained low-pressure volumes are (given bridgmanite's stability limit), forcing the model to rely heavily on the V_0 prior.

Focusing on the highly correlated pairs of *cold* and *thermal* parameters, Figure 6 shows the correlated 68% confidence regions for (K_{0T}, K'_{0T}) and (γ_0, q). The 13% Fe-bearing bridgmanite measured in this study is shown in red, while the Fe-free bridgmanite from *Tange et al.* [2012] is in black. From these confidence regions, we clearly see that the major cold and thermal parameters of bridgmanite are significantly influenced by the addition of iron, as demonstrated by the wide separation of these confidence ellipses. Also displayed as a black cross is the reported best-fit values from *Tange et al.* [2012], which should nominally lie at the center of the black confidence ellipses. The cold parameter offset is primarily caused by Tange's fixing of V_0 to its measured value (while the source of the hot parameter offset is unclear).

Previous x-ray diffraction studies of Fe-free bridgmanite have typically reported a range of isothermal bulk moduli that have smaller values than reported here, including: 252 ± 5 GPa from *Lundin et al.* [2008], 253-259 GPa from *Fiquet et al.* [2000] depending on whether heated data was included in the fit, and 259.6 ± 2.8 GPa from *Mao et al.* [2011]. All of these studies, however, fixed the value of V_0 to a measured volume, rather than using a prior to loosely constrain its behavior. Both Tange's measured zero-pressure volume

(162.373 $\mathring{A}^3$) and the typical measured value (162.5 $\mathring{A}^3$, see Figure 3) exceed our fitted value ($162.12 \pm 0.13 \mathring{A}^3$) by about 2σ and 3σ, respectively, indicating that the behavior of bridgmanite outside its stability field deviates significantly from its high-pressure behavior, affecting both volumes and compressibilities. If we compute the conditional equation of state parameters for Fe-free bridgmanite (fixing V_0 to its most typical measured value of 162.5 $\mathring{A}^3$), we get a low-pressure appropriate bulk modulus of $K_{0T} = 253.2 \pm 4.4$ GPa, in general agreement with previous diffraction studies. The accuracy of this low pressure prediction can be tested most effectively by comparing it with the direct adiabatic bulk modulus determinations made from low-pressure Brillouin spectroscopy measurements like those of *Sinogeikin et al.* [2004], who reported a zero-pressure adiabatic bulk modulus of 253 ± 3 GPa for single crystal Fe-free bridgmanite. To compare with this measurement, we calculate the adiabatic bulk modulus from the thermodynamic relation $K_S = K_T(1 + \alpha\gamma T)$. Evaluated at zero pressure and 300 K, this yields a value of $K_{S0} = 255.7 \pm 4.4$ GPa for Fe-free bridgmanite, which is nicely consistent with the direct metastable measurement.

These measurements show that ferrous iron substitution affects not only the 300 K elastic properties of bridgmanite, but the high-pressure *thermal* parameters as well (see Figure 6b). The 68% confidence regions for γ_0 and q for Fe-bearing and Fe-free bridgmanite do not overlap one another, indicating that both γ_0 and q drop a statistically significant amount with the addition of 13% iron. Since the thermal pressure term is roughly linear in the Grüneisen parameter (see Equation 3), this change implies a drop in the thermal pressure component at ambient conditions, coupled with a slower decrease associated with compression. Equivalently, this be seen as a pressure-dependent reduction in thermal expansion, since neighboring isotherms are closer to one another, evolving

from a ∼14% drop in α at 24 GPa to equal values at ∼100 GPa when evaluated along a mantle geotherm. Though there are many studies available on the low-pressure thermal expansion properties of Fe-free and Fe-bearing bridgmanite [i.e. *Knittle et al.*, 1986; *Wang et al.*, 1994; *Anderson*, 1998], they are dominated by measurements of bridgmanite outside its thermodynamic stability field, hindering reliable comparison with this high-pressure study. In fact, the contrast between high- and low-pressure bridgmanite vibrational properties were directly established through Raman spectroscopy by *Chopelas* [1996], who showed that bridgmanite's vibrational frequency compression trends posses a strong kink at about ∼40 GPa. (The vibrational modes responsible for this change may actually play a role in destabilizing bridgmanite relative to its lower pressure polymorphs.) Such a change in phonon frequency evolution implies changes in thermal properties, like thermal expansion, as well as static compression properties like the bulk modulus, supporting the idea that thermodynamically metastable bridgmanite behaves quite differently from stable bridgmanite.

To explore the robustness of our conclusions, we must revisit our assumption about the composition-independence of the reference Debye temperature. While the available experimental evidence supporting this assumption is somewhat weak, we can assess its plausibility using theoretical calculations. From the formalism of *Anderson et al.* [1992], we can determine the relative affect of ferrous iron on the Debye temperature, which is proportional to both the Debye sound velocity and the inverse linear compression ratio $(V/V_0)^{-1/3}$. The volume change associated with increasing bridgmanite's iron composition from 0% to 13% is only 0.4%, so the linear compression ratio in this case has negligible effect on the Debye temperature. The Debye sound velocity is a weighted average of

both the compressional and shear wave velocities, which can be determined from first-principles phonon calculations. Using density functional theory, *Kiefer et al.* [2002] and *Metsue and Tsuchiya* [2012] found that incorporation of 25% ferrous Fe into bridgmanite induces only a modest change in the sound velocities of $\Delta V_p/V_p \approx -4\%$ and $\Delta V_s/V_s \approx -6\%$, corresponding to a drop of roughly $\sim$5% in the Debye sound velocity and the associated Debye temperature. For 13% Fe-bearing bridgmanite, we expect an effect only half this size, yielding a shift of only $\Delta\Theta_0\sim$ -25 K as compared to Fe-free bridgmanite; this small shift is well within the 77 K uncertainties for the iron-free endmember model and can be safely ignored. This theory-based reasoning is consistent with the acoustic measurements of *Lu et al.* [1994], which were unable to resolve a difference between Fe-free and 10% Fe-bearing bridgmanite. Furthermore, the measurements of *Murakami et al.* [2012] and *Jackson et al.* [2004, 2005] on Al-bearing and Mg end-member bridgmanite also showed a small drop in shear wave speeds of less than 3%, supporting the conclusion that bridgmanite's rough zero-pressure lattice dynamical properties are not highly sensitive to minor cation substitutions.

4.3. Confidence Bounds on High-Pressure Thermal Properties

While considerable attention is often given to directly comparing equation of state parameter values, in reality, we are most interested in the behavior of bridgmanite at mantle-relevant P-T conditions, rather than the room pressure-temperature conditions where the parameters are defined. We thus propagate our EOS model uncertainties (given by the covariance matrices) to determine confidence bounds on the thermophysical properties at elevated pressure-temperature states. In the upper panel of Figure 7, we plot the 68% confidence regions on a set of isotherms for the two bridgmanite samples. Direct compar-

ison of the low temperature Fe-bearing and Fe-free isotherms shows the reducing effect of iron on the bulk modulus, yielding a more compressible crystal that undergoes a volume crossover with iron-free bridgmanite at about 40 GPa at 300 K. Iron's influence on the thermal expansion is also visible in the spacing of adjacent isotherms, which is significant below 60 GPa but weakens with increasing pressure. From these confidence bounds, it is clear that the high pressure properties of both Fe-free and Fe-bearing bridgmanite are well constrained throughout the lower mantle P-T range, especially near the core-mantle boundary.

To further investigate how these materials might behave at deep mantle conditions, we also estimate the confidence intervals for a representative mantle geotherm. We calculate these profiles (Figure 7 & Table 5) by combining a self-consistent adiabat, chosen to match the 1873 K mantle adiabat (defined at 670 km) from *Brown and Shankland* [1981], with an added thermal boundary layer up to a nominal CMB temperature of 4000 K. This approach is consistent with recent mantle geotherms presented in *Stixrude and Lithgow-Bertelloni* [2007] and *Stixrude et al.* [2009]. The resulting bridgmanite-only geotherms and the associated material property profiles, are given in Table 5 for both the 13%-Fe and Fe-free compositions. To visually compare these profiles with bulk mantle values represented by the Preliminary Reference Earth Model (PREM) [*Dziewonski and Anderson*, 1981], we determine the 68% confidence bounds on the density and adiabatic bulk modulus and plot their lower mantle PREM anomalies in the lower panel of Figure 7. The important takeaway from this figure is that although the addition of iron dramatically increases density, it has only marginal statistically significant impact on the high P-T

compressibility in the lowermost mantle, as demonstrated by the near total overlap of the Fe-bearing and Fe-free confidence intervals above ∼70 GPa.

5. Geophysical Implications

To explore the thermophysical properties of Mg-Fe bridgmanite at arbitrary iron compositions, we construct an ideal lattice mixing model based on the equation of state properties determined for 0% and 13% Fe-containing bridgmanite.

5.1. Assessing a Bridgmanite-Dominated Lower Mantle

Though most compositional models of the lower mantle include a significant compliment of other phases, including about ∼15-20% ferropericlase and a few percent $CaSiO_3$ perovskite [e.g. *Irifune*, 1994; *Irifune et al.*, 2010; *Stixrude and Lithgow-Bertelloni*, 2011], there are many uncertainties and underlying assumptions that go into constructing these models. This view has been challenged by previous authors, including *Stixrude et al.* [1992] and *Murakami et al.* [2012], who put forward a simpler compositional model involving a bridgmanite-dominated lower mantle. *Murakami et al.* [2012] suggested that the lower mantle may be composed of nearly pure bridgmanite (>93%) based upon its match to seismic shear-wave velocities from PREM. Given the equation of state models developed here, we are well positioned to further explore this possibility.

In place of the familiar ideal mixing model, where volumes mix linearly in composition at constant (P & T), we employ an ideal lattice mixing model more appropriate to solid solutions. In this framework, energies of the reference components are combined linearly in composition, implying linear behavior in both energy and its volume-derivative (pressure),

yielding the following simple expression:

$$P(X,V,T) = \frac{X}{0.13}P_{\mathrm{MgFe}}(V,T) + \frac{0.13-X}{0.13}P_{\mathrm{Mg}}(V,T) \quad (13)$$

where $P_{\mathrm{MgFe}}(V,T)$ and $P_{\mathrm{Mg}}(V,T)$ are the calculated pressures for 13% and 0% Fe-bearing bridgmanite, as determined in this study. The Mie-Grüneisen-Debye equation of state at arbitrary composition is then determined by fitting ideal model pressures over a grid of volumes and temperatures (120 to 200 $\mathring{A}^3$ and 300 to 5000 K). This type of ideal mixture, which is carried out at constant V and T, accounts for the energetic cost of straining the end-members to a common lattice volume prior to mixing, which can contribute significantly to apparent "non-ideal" behavior [e.g. *Vinograd and Sluiter*, 2006]. In this application, a common volume is required for Mg and Fe atoms to share the same bridgmanite crystal lattice, and this simple approach automatically incorporates the lattice strain energy without needing to introduce any regular solution parameters.

The results of this mixture model comparison are given in Figure 8, where we examine the material properties of bridgmanite at deep-mantle conditions. We construct representative geothermal profiles as in the previous section by combining self-consistent adiabats with an added thermal boundary layer, as depicted in Figure 8a. Since both composition and temperature of the deep mantle remain fairly uncertain, we consider a range of possible values, allowing the geotherm to be elevated relative to the representative mantle geotherm, shown in gray, based on the 1873 K adiabat from *Brown and Shankland* [1981]. The excess temperature, ΔT_{ex} is defined as the adiabatic temperature difference from the reference adiabat at 120 GPa, just outside the thermal boundary layer. By repeating this calculation for a range of possible compositions and excess temperatures, we can explore the role that both variables play in determining lower mantle properties. Figure 8b shows

density and bulk modulus anomalies relative to PREM at 120 GPa by solid and dashed contours, respectively. The figure confirms that bridgmanite has a high relative bulk modulus over nearly the entire range of plausible temperatures and compositions, indicated by the orange and red dashed contours. Density, on the other hand, is more sensitive to composition, where the zero-anomaly line shown in solid gray increases from about 9% to 15% Fe content as the assumed excess temperature is raised by 1500 K. Even over this wide range of possible lower-mantle adiabatic temperatures, there is no bridgmanite composition that can satisfy both the density and bulk modulus of the average mantle, as indicated by the non-intersection of the gray dashed and solid zero-anomaly lines. This analysis of density and compressibility anomalies thus disagrees with the findings of *Murakami et al.* [2012], which preferred a nearly pure bridgmanite mantle based upon its agreement with seismic shear-wave velocities.

5.2. Bridgmanite-Dominated Chemical Piles

The composition-dependent bridgmanite equation of state developed above is also useful in assessing the relative merits of different possible explanations for the Large Low Shear Velocity Provinces (LLSVPs). Under the umbrella of chemically distinct explanations for these lower mantle structures, there are two broad endmember theories that account for their large topographic relief relative to the CMB [*Tan and Gurnis*, 2007; *Garnero and McNamara*, 2008]. At one extreme, they might represent chemically dense *passive* piles, which are dynamically propped up by external convective stresses, while at the other, they could be free-standing and internally convecting *metastable* piles, whose topography is a direct reflection of the thermophysical properties of the pile material.

747 The passive pile explanation is the more intuitive of the two, in which the piles reside at
748 the base of the mantle reflecting their greater chemical density. Fighting their tendency
749 to spread out and pool as thin shallow layers on the CMB, some external force must be
750 invoked to sweep them into domed piles, such as cold dense plates descending to the CMB
751 and pinching the sides of these structures in order to dynamically prop them up [*Bower*
752 *et al.*, 2013]. This story assumes a sufficient plate-flux at the CMB with appropriate
753 geometry to provide the needed lifting force to counteract the pile's negative chemical
754 buoyancy. Under the competing scenario, no external force is required, but rather the
755 chemically distinct piles are made of a material that is less dense than the surrounding
756 mantle at the base but experiences a density crossover, or height of neutral buoyancy,
757 near the top of the pile about 1000 km above the CMB. Under this explanation, the
758 pile undergoes internal convection with hot low-density material rising from the thermal
759 boundary layer at the base of the pile toward a neutral buoyancy point, where it cools
760 and falls back to the CMB enabling the pile to prop itself up without the help of external
761 stresses. This behavior clearly depends on both the thermal structure of the pile as well
762 as its thermophysical properties, which depend on composition.

763 Though we have little knowledge about of the detailed composition of LLSVPs, one
764 possible model for such structures is a dome composed primarily of bridgmanite. While
765 the bulk mantle likely boasts a $(Mg, Fe)O$ ferropericlase component of roughly 15-20% (by
766 volume) and lesser amount of $CaSiO_3$ perovskite [e.g. *Irifune*, 1994; *Irifune et al.*, 2010;
767 *Stixrude and Lithgow-Bertelloni*, 2011], the pile material must be exceptionally incom-
768 pressible in order to produce a neutrally buoyant self-supporting structure. This requires
769 a much higher contribution from a silica-rich phase like bridgmanite, since $(Mg, Fe)O$ is

more compressible than its co-existing silicates and calcium silicate perovskite is thought to have a bulk modulus lower than bridgmanite and about equal to that of PREM. It is therefore useful to consider the limiting case of a pile made entirely of Fe-bearing bridgmanite. The possibility of bridgmanite-dominated LLSVPs was explored in *Dorfman and Duffy* [2014], by approximating chemical and thermal effects as independent, noting that observed density anomalies are plausibly explained by iron-enrichment. With the high-temperature equation of state information obtained in this study, we can investigate this possibility in greater detail, allowing for chemistry-dependent thermal effects to alter the pile's buoyant stability.

In order to model the LLSVPs, we calculate geothermal profiles for pure bridgmanite layers and compare relative density anomalies as a function of pressure. Figure 9a shows a few sample calculations of the geothermal trend for bridgmanite with an elevated temperature of $\Delta T_{\mathrm{ex}} = 900$ K above the average mantle profile for a range of iron compositions. Confirming intuition, the plot demonstrates that adding iron increases the density of the bridgmanite layer, taking it from buoyantly unstable at 11%, with a density everywhere lower than bulk mantle values, to a dense stable layer at 13%, with a higher than average density over most of the lower mantle. The curve corresponding to 12% Fe shows the qualitatively different case of a neutrally buoyant structure, that is less dense than average mantle at the CMB, but undergoes a density crossover at mid-mantle depths due to its high bulk modulus. This special case corresponds to the metastable dome model for LLSVPs suggested by *Tan and Gurnis* [2007].

Using the same geotherm comparison procedure, we can predict the expected heights of neutral buoyancy for a bridgmanite-only pile in the deep mantle. First we focus in on the

expected temperature contrast for LLSVPs relative to average mantle, which are estimated from seismic tomography models and geodynamic simulations to be roughly 1000 K [*Tan and Gurnis*, 2007; *Bower et al.*, 2013]. Panel b of Figure 9 maps out this parameter space by noting the relative buoyant stability of the structure as a function of composition and temperature, where the pink shading denotes the metastable dome region with neutral buoyancy heights falling between 600 and 1200 km above the CMB, generally matching the observed LLSVP heights. The green shaded region to the left contains piles that extend too high above the CMB or are fully unstable to convection, while the unshaded region to the right corresponds to dense passive piles that rely on viscous stresses to dynamically prop them up off the CMB. For comparison, the CMB density contours from Figure 8 are also shown indicating anomalies between -3 and +3%, which reflect the maximum plausible range of density differences based on seismic observations (such as the normal mode inversion of *Ishii and Tromp* [1999]).

As is clear from the figure, there is only a tiny sliver of allowable phase space that corresponds to the delicate balance required by the metastable dome hypothesis. In contrast, passive piles are extremely insensitive to composition and temperature. We can thus assess the relative plausibility of the passive pile and metastable dome explanations by calculating the fraction of allowable phase space occupied by the two theories—this is given simply by the relative area of the red-shaded and unshaded regions falling within the desired maximum density anomaly contour. This probability fraction is only $\mathcal{P}\sim4\%$ for up to 3% density anomalies (or $\mathcal{P}\sim7\%$ if restricted to 1.5% anomalies), indicating that while metastable domes are possibly consistent with our current understanding of the bridgmanite equation of state, they imply very tight constraints on the temperature-

dependent composition of the LLSVP material and are thus highly unlikely. Furthermore, we recognize that the positive slope of this metastable region places strong restrictions on the allowable thermal evolution of a metastable dome. If the pile is buoyantly metastable, then it must have remained stable since its creation early in Earth's history, meaning that it could not have had greater thermal contrast in the distant past. We can thus rule out any formation scenarios that would produce increased thermal anomalies early on, even if they might result in a metastable structure today. For instance, the layer cannot contain an increased concentration of radiogenic heat-producing elements, since this would cause it to heat up rendering it unstable. Similarly, an increased core-mantle boundary heat flux early on could also make it difficult to form a long-lived metastable pile, since any initially metastable structure would gradually cool relative to the mantle, evolving into a passive chemically dense layer. These constraints on relative thermal evolution cast further doubt onto the metastable dome hypothesis.

In this analysis, we consider a pure simplified bridgmanite chemistry, neglecting the roles of other phases like ferropericlase, calcium silicate perovskite, aluminum-bearing phases or basaltic components, or post-bridgmanite. As stated above, the addition of ferropericlase, which has a lower high-pressure bulk modulus lower than bridgmanite, would render metastable domes more difficult to form, since a high bulk modulus is needed to provide convective self-support. Post-bridgmanite is also neglected since it would only play a potential role at the very base of the LLSVP, and its positive Clapeyron slope diminishes its importance within hot LLSVPs due to the increased transition pressure. Given our simplified compositional model as a foundation, the possible effects of a more realistic bridgmanite chemistry is certainly worth exploring. We can estimate the effect

of substituting 10% Al into bridgmanite using the Fe, Al-bridgmanite equation of state of *Catalli et al.* [2011], which showed a roughly 4% drop in the bulk modulus and density. For the most part, this would merely increase the bulk modulus and density values and would therefore shift the metastable dome region toward higher iron contents, but would not significantly alter its size. We thus conclude that aluminum should have little affect on either the assessment of a bridgmanite-dominated lower mantle or in the likelihood of dynamically metastable LLSVPs.

6. Conclusion

Iron-bearing magnesium silicate perovskite (or bridgmanite) is thought to make up most of the Earth's lower mantle, enabling it to exert strong controls over lower mantle dynamics and thermodynamics. Laser-heated diamond anvil cell experiments are performed using a nearly hydrostatic neon pressure medium to determine the thermal equation of state of synthetic 13% Fe-bearing ferrous $(Mg, Fe)SiO_3$ bridgmanite. We combine this new dataset with the sintered diamond multi-anvil and diamond anvil cell measurements of a pure $MgSiO_3$ bridgmanite sample reported in *Tange et al.* [2012] to determine the effect of ferrous iron on the high P-T behavior of bridgmanite. These data are fit with a Mie-Grüneisen-Debye equation of state, using a novel Bayesian error-modeling procedure (implemented in a publicly-available MATLAB code **pvt-tool**, *http://github.com/aswolf/pvt-tool*) to determine accurate parameters along with their correlated uncertainties. Particular care is taken to investigate the possible differences between the high-pressure behavior of bridgmanite, most relevant to the Earth's mantle, and its low-pressure metastable behavior observed in many past experiments. Through this analysis, we find evidence that metastable bridgmanite shows distinctly different properties outside its thermodynamic

stability field, including its overly large zero-pressure volume and associated higher compressibility. To account for these changes, we show that fixing V_0 to measured zero-pressure volumes produces isothermal and adiabatic bulk moduli values that are fully consistent with previous equation of state studies and direct sound-velocity based measurements.

The high-pressure equations of state for 13%-Fe and Fe-free bridgmanite are incorporated into an ideal lattice mixing model enabling the estimation of thermophysical properties for a large range of ferrous iron compositions. Using this mixture model, we examine the range of plausible values in temperature-composition space relevant to the deep mantle. Through this analysis, we demonstrate that there is no combination of temperature and composition capable of matching the Earth's bulk properties near the base of the mantle, ruling out the possibility of a pure bridgmanite lower mantle composition. Furthermore, we explore the buoyancy properties of bridgmanite-dominated piles in the deep mantle, directly relevant to Large Low Shear Velocity Provinces. Using plausibility arguments, we show that metastable bridgmanite domes are marginally possible, given our knowledge of the equation of state, but represent a sensitive balance between iron content and temperature, and are therefore unlikely. Instead, we find the passive chemical pile explanation more compelling, as it allows for a broad range of composition and temperature values in the deep mantle, but may require external forces to sweep them into coherent structures.

Appendix A: Data Reduction Pipeline

Raw powder diffraction images are converted to one-dimensional patterns using a suite of routines written in MATLAB. In these routines, the observing geometry is first determined from calibration diffraction images using an automated statistical method. This has the

advantage over the standard 'click-based' method employed in FIT2D that it requires little user input and generates a reproducible result using maximum likelihood estimation of the observing geometry from calibration image data. With the derived geometric calibration, the observed diffraction angle (2θ) is calculated for each pixel on the CCD. Diffraction angle is converted to inverse d-spacing ($1/d$) by applying Bragg's law for first-order reflections, $1/d = 2\sin(2\theta/2)/\lambda$, where d is the distance between coherently reflecting lattice planes, and λ is the wavelength of the monochromatic x-rays used to probe the sample. Each raw image is then *integrated* assuming Poisson statistics for the uncertainties in number of photons hitting each pixel. For some of the diffraction images, which contain over-exposed pixels, a further preprocessing step is required to produce accurate 1-D patterns (discussed below). The final step in the integration process is to subtract off an initial estimate of the background intensity so that datasets can be easily examined and fit. We employ the Bayesian background identification and subtraction method presented in *David and Sivia* [2001], which automatically determines a reasonable polynomial background curve assuming the potential presence of large positive deviations due to as-yet unmodeled diffraction peaks.

We determine the detector geometry using a method similar to that reported in [*Hinrichsen*, 2006]. After determining an approximate beam-center location, the diffraction data for a known calibration standard–such as CeO_2 or LaB_6–is sliced radially using bi-cubic interpolation to obtain a set of 1-D radial pattern. Peak fitting with pseudo-Voigt profiles is then used to extract the 2θ locations of every line in each radial slice. These calibration line positions (with associated uncertainties) are then fit by varying the experimental geometry parameters controlling the orientation and position of the detector: detector

distance, beam-center location, and detector tilt and rotation. The geometric calibration parameters are chosen as the values with the maximum likelihood given the measured line positions using the standard least-squares method (as is appropriate to simple data fitting with Gaussian uncertainties and in the absence of strong prior information).

For diffraction images containing both strong and weak x-ray scatterers, it is often impossible to obtain high quality patterns that do not suffer from over-exposure in certain regions of the image. Due to the basic properties of CCD detectors, exposure of a pixel beyond its full-well depth causes 'blooming' in the final image, where electrons spill over into neighboring pixel wells causing full-intensity streaks to emanate from the excessively bright points in the image. The typical approach to this problem is to adjust exposure times to limit its occurrence. Unfortunately, in many cases this method is either ineffective (e.g., in the presence of very weak scatterers) or impractical (e.g., during high-temperature measurements). It would be highly advantageous to be able to use these data while minimizing the impact of the erroneous intensities caused by blooming–such an approach is made possible by the conservation of electrons within the affected region. Since the total number of electrons, equal to the number of photons registered by the CCD, remains constant as electrons spill into neighboring pixel bins, simple summation in an overexposed region will give an approximate total intensity for that region. In order to determine how to reasonably distribute this total amongst the affected pixels, we leverage the angular symmetry inherent to powder diffraction by setting the relative intensity of each pixel to the values from integrated 1-D pattern. Iterating this procedure then results in reasonable pixel intensities which will no longer induce wild bias into the final integrated pattern.

928 The final data reduction step is the integration procedure itself, which operates on
929 the powder diffraction images (pre-corrected for saturation if necessary) using the geo-
930 metric parameters derived from the calibration image. Using the equations presented in
931 *Hinrichsen et al.* [2008], we determine the proper intensity weighting factors required to
932 transform each measured pixel value into an equivalent ideal pixel intensity for a per-
933 pendicular and hemispherical detector. This factor is combined with the standard 2-D
934 Lorentz and polarization correction factors (see, e.g., *Hinrichsen et al.* [2008]), forming a
935 single overall weighting factor for each pixel on the detector. Since this intensity weighting
936 map is independent of the data collected, it need only be calculated once for each detector
937 configuration. To obtain a reasonably smooth one-dimensional pattern, as remarked by
938 *Hammersley et al.* [1996], measured pixel intensities are divided amongst sub-pixel regions
939 according to standard bi-cubic interpolation. These sub-pixels are then sorted into bins
940 according to their diffraction angle 2θ. The sub-pixel intensities are combined together
941 as weighted observations of a Poisson process, using the intensity weight map described
942 above, resulting in a one-dimensional pattern of intensity as a function of diffraction angle.
943 After the integration, we apply the method derived by *David and Sivia* [2001] to estimate
944 and subtract a robust Chebyshev polynomial background from the pattern. This acts as
945 a good initial guess of the background, which can later be refined, and provides a simple
946 flat pattern ready for analysis and visualization.

Appendix B: Extracting Crystal Volumes and Cell Dimensions

After obtaining line position estimates from the powder diffraction pattern, the next step is to fit these positions with a crystal lattice model to estimate unit cell dimensions and volumes. As an orthorhombic crystal, the predicted peak positions are a simple function

of the lattice parameters and the hkl values for each reflection in the bridgmanite pattern:

$$\left(\frac{1}{d}\right)^2 = \left(\frac{h}{a}\right)^2 + \left(\frac{k}{b}\right)^2 + \left(\frac{l}{c}\right)^2 \tag{B1}$$

where hkl are the reflection order parameters, abc are the crystal unit cell parameters, and d is the atomic plane spacing. Using this model for the 10 to 25 identified peak positions, we obtain an initial guess for the unit cell parameters by fitting the volume $V = abc$, and axial ratios ((c/a) and (b/a)) using standard weighted least-squares regression, where the uncertainties for each peak are determined from the empirical scatter of the measurements about the best-fit smooth (quadratic) trend with pressure. Subsequently, we carry out a more careful Bayesian analysis that accounts for the potential presence of misidentified lines and determines realistic estimates of the unit cell parameters along with their correlated uncertainties. Additionally, we make use of the ambient pressure relative peak intensities, obtained from the crystal model of *Sugahara et al.* [2006], as rough order-of-magnitude guide for which lines most likely dominate the diffraction pattern over the full range of pressures and temperatures.

In order to address line misidentification, we use a simple Bayesian mixture model approach, which is robust against moderate degrees of contamination by peak identification errors. This general statistical tool is useful in analyzing "polluted" datasets where there are a variety of possible data sources, such as bona fide bridgmanite peaks together with unwanted misidentified peaks. (See section 8.3 of *Sivia and Skilling* [2006] for a useful and succinct general discussion of the importance of properly handling outliers in generic data analysis applications.) To account for the contribution of misidentified peaks, we assume that each position measurement is drawn at random from one of two possible populations: either it is properly identified and drawn from the true sample line

968 population or it is misidentified and draw from a population of confused lines. As with
969 the standard least squares approach, properly identified peaks are considered normally
970 distributed about the model value with uncertainties given by the line position errors.
971 The confused line population is represented with a flat distribution centered on the ex-
972 pected position with a width of Δp, corresponding to how closely spaced observed and
973 predicted line positions must fall in order for misidentification to occur. We estimate a
974 reasonable value for the width of $\Delta p \approx 0.02$, which is roughly a few times larger than
975 the typical uncertainties on line position. The total likelihood for each data point is just
976 a *mixture*, or a weighted average, of these two distributions [*Sivia and Skilling*, 2006]:
977 $\mathcal{L} = \prod_i \left((1-f)\mathcal{N}(p_i - p_i^{\rm mod}, \sigma_i) + \frac{f}{\Delta p}\right)$, where f is the expected fraction of the data
978 points that are incorrectly identified. When there are no misidentified peaks, $f = 0$ and
979 we recover the standard least-squares approach. Taking the negative log of this expres-
980 sion, we obtain the *goodness-of-fit* metric to be minimized, akin to χ^2, for the Bayesian
981 mixture model:

$$-\log \mathcal{L} = -\sum_i \log\left(\frac{(1-f)}{\sqrt{2\pi}\sigma_i}\exp\left[-0.5\left(\frac{p_i - p_i^{\rm mod}}{\sigma_i}\right)^2\right] + \frac{f}{\Delta p}\right) \quad \text{(B2)}$$

983 We assume a modest degree of contamination from misidentified lines ($f = 0.1$), though
984 the results are fairly insensitive to its exact value as long as it is nonzero. This goodness-
985 of-fit equation is then used in conjunction with the line position model to obtain a robust
986 fit to the observed line positions.

987 Though we present peak identification and crystal modeling in two separate sections,
988 in truth there exists large overlap between the two. Peak identification and fitting is
989 inherently an iterative process, where peak identification improves as the model is refined

with the addition of each new peak. At the same time, however, the addition of an incorrect peak at such an early stage can be quite detrimental when using the standard least-squares approach. The Bayesian mixture model significantly reduces the effect of the misidentified peaks on the overall fit, making it useful both for obtaining final estimates as well as early on in the peak identification and fitting process.

Uncertainties for the inferred bridgmanite volumes are obtained by propagating the uncertainties in the individual line positions. Thus far, we have roughly estimated line position errors based on the observed scatter about a smooth pressure trend. This is a reasonable approach, but is limited to ambient temperature measurements. Additionally, it also folds extra scatter due to pressure uncertainties back into the line position errors, essentially double-counting the pressure errors. We can handle both of these limitations by instead examining the scatter of the line positions in an entirely geometric space independent of pressure. Unit analysis and inspection of Equation (B1) suggests that the line positions, $1/d$, behave smoothly when plotted against the inverse average cell dimension, $1/\langle a \rangle = V^{-1/3}$, resulting in linear behavior that is independent of temperature, due to its purely geometric construction. To further improve the model, we also assume that the error on each individual line is roughly proportional to peak width ($\sigma_i = \alpha w_i$), as this is the primary variable controlling the ability to determine the location of a peak assuming it is clearly visible. The constant of proportionality, α, is specific to each line, and determined empirically using the scatter of peak positions about their linear trend with compression. By scaling all of the line-specific constants of proportionality, we ensure that the observed scatter is well explained by the inferred line position errors. Obtaining a final uncertainty on the volume and axial ratios now reduces to the usual approach of

calculating standard errors from the curvature of the goodness-of-fit in parameter space (in this case, using the Bayesian mixture model rather than χ^2 to obtain robust error estimates).

Acknowledgments. The authors would like to thank Wolfgang Sturhahn, June K. Wicks, Dan J. Bower, Mike Gurnis, Jeroen Ritsema, and John Johnson for useful conversations throughout the development of this study, as well as both reviewers for their detailed and helpful comments. The authors would like to thank the National Science Foundation CSEDI EAR-1161046, CAREER EAR-0956166, and the Turner Postdoctoral Fellowship at the University of Michigan for support of this work. The x-ray diffraction experiments were performed at GeoSoilEnviroCARS (GSECARS, Sector 13) and the synchrotron Mössbauer experiments at X-ray Science Division (Sector 3), both located at the Advanced Photon Source (APS), Argonne National Laboratory. GeoSoilEnviroCARS is supported by the National Science Foundation - Earth Sciences (EAR-1128799) and Department of Energy - Geosciences (DE-FG02-94ER14466). Use of the APS is supported by the U.S. D.O.E., O.S., and O.B.E.S. (DE-AC02-06CH11357). Sector 3 operations and the gas-loading system at GSECARS are supported in part by COMPRES under NSF Cooperative Agreement EAR 11-57758. The data analyzed in this study are included in the tables; any additional data may be obtained from Aaron S. Wolf (aswolf@umich.edu).

References

Alp, E., W. Sturhahn, and T. Toellner (1995), Synchrotron Mossbauer spectroscopy of powder samples, *Nuclear Instruments and Methods in Physics Research Section B: Beam Interactions with Materials and Atoms*, *97*(1-4), 526–529.

1034 Anderson, O. L. (1998), Thermoelastic properties of MgSiO 3 perovskite using the Debye
1035 approach, *American Mineralogist*, *83*(1-2), 23–35.

1036 Anderson, O. L., D. Isaak, and H. Oda (1992), High-temperature elastic constant data on
1037 minerals relevant to geophysics, *Rev. Geophys.*, *30*(1), 57–90.

1038 Andrault, D., N. Bolfan-Casanova, M. Bouhifd, N. Guignot, and T. Kawamoto (2007),
1039 The role of Al-defects on the equation of state of Al-(Mg,Fe)SiO3 perovskite, *Earth and*
1040 *Planetary Science Letters*, *263*(3-4), 167–179.

1041 Ballaran, T. B., A. Kurnosov, K. Glazyrin, D. J. Frost, M. Merlini, M. Hanfland, and
1042 R. Caracas (2012), Effect of chemistry on the compressibility of silicate perovskite
1043 in the lower mantle, *Earth and Planetary Science Letters*, *333-334*(0), 181–190, doi:
1044 10.1016/j.epsl.2012.03.029.

1045 Bengtson, A., J. Li, and D. Morgan (2009), Mössbauer modeling to interpret the spin
1046 state of iron in (Mg,Fe)SiO3 perovskite, *Geophys. Res. Lett.*, *36*(15), L15,301–.

1047 Bower, D. J., M. Gurnis, and M. Seton (2013), Lower mantle structure from paleogeo-
1048 graphically constrained dynamic Earth models, *Geochem. Geophys. Geosyst.*, *14*(1),
1049 44–63.

1050 Brown, J. M., and T. J. Shankland (1981), Thermodynamic parameters in the Earth
1051 as determined from seismic profiles, *Geophysical Journal of the Royal Astronomical*
1052 *Society*, *66*(3), 579–596.

1053 Burke, K., B. Steinberger, T. H. Torsvik, and M. A. Smethurst (2008), Plume Genera-
1054 tion Zones at the margins of Large Low Shear Velocity Provinces on the core-mantle
1055 boundary, *Earth and Planetary Science Letters*, *265*(1-2), 49–60.

Catalli, K., S.-H. Shim, V. Prakapenka, J. Zhao, and W. Sturhahn (2010a), X-ray diffraction and Mössbauer spectroscopy of Fe3+-bearing Mg-silicate post-perovskite at 128–138 GPa, *American Mineralogist*, *95*(2-3), 418–421, doi:10.2138/am.2010.3352.

Catalli, K., S.-H. Shim, V. B. Prakapenka, J. Zhao, W. Sturhahn, P. Chow, Y. Xiao, H. Liu, H. Cynn, and W. J. Evans (2010b), Spin state of ferric iron in MgSiO3 perovskite and its effect on elastic properties, *Earth and Planetary Science Letters*, *289*(1-2), 68–75.

Catalli, K., S.-H. Shim, P. Dera, V. B. Prakapenka, J. Zhao, W. Sturhahn, P. Chow, Y. Xiao, H. Cynn, and W. J. Evans (2011), Effects of the Fe3+ spin transition on the properties of aluminous perovskite—New insights for lower-mantle seismic heterogeneities, *Earth and Planetary Science Letters*, *310*(3-4), 293–302, doi:10.1016/j.epsl.2011.08.018.

Chantel, J., D. J. Frost, C. A. McCammon, Z. Jing, and Y. Wang (2012), Acoustic velocities of pure and iron-bearing magnesium silicate perovskite measured to 25 GPa and 1200 K, *Geophys. Res. Lett.*, *39*(19), L19,307–.

Chopelas, A. (1996), Thermal expansivity of lower mantle phases MgO and MgSiO3 perovskite at high pressure derived from vibrational spectroscopy, *Physics of the Earth and Planetary Interiors*, *98*(1-2), 3–15.

Cohen, R. E., O. Gülseren, and R. J. Hemley (2000), Accuracy of equation-of-state formulations, *American Mineralogist*, *85*(2), 338–344.

Daniel, I., J. D. Bass, G. Fiquet, H. Cardon, J. Zhang, and M. Hanfland (2004), Effect of aluminium on the compressibility of silicate perovskite, *Geophys. Res. Lett.*, *31*(15), L15,608–.

Datchi, F., R. LeToullec, and P. Loubeyre (1997), Improved calibration of the SrB4O7:Sm2+ optical pressure gauge: Advantages at very high pressures and high temperatures, *Journal of Applied Physics*, *81*(8), 3333–3339, doi: http://dx.doi.org/10.1063/1.365025.

Datchi, F., A. Dewaele, Y. Le Godec, and P. Loubeyre (2007), Equation of state of cubic boron nitride at high pressures and temperatures, *Phys. Rev. B*, *75*(21), 214,104–.

Davaille, A., E. Stutzmann, G. Silveira, J. Besse, and V. Courtillot (2005), Convective patterns under the Indo-Atlantic ¡¡ box ¿¿, *Earth and Planetary Science Letters*, *239*(3-4), 233–252.

David, W. I. F., and D. S. Sivia (2001), Background estimation using a robust Bayesian analysis, *Journal of Applied Crystallography*, *34*(3), 318–324, doi: doi:10.1107/S0021889801004332.

Davies, D. R., S. Goes, J. Davies, B. Schuberth, H.-P. Bunge, and J. Ritsema (2012), Reconciling dynamic and seismic models of Earth's lower mantle: The dominant role of thermal heterogeneity, *Earth and Planetary Science Letters*, *353-354*(0), 253–269.

Dewaele, A., F. Datchi, P. Loubeyre, and M. Mezouar (2008), High pressure–high temperature equations of state of neon and diamond, *Phys. Rev. B*, *77*(9), 094,106–9.

Dorfman, S., and T. Duffy (2014), Effect of Fe-enrichment on seismic properties of perovskite and post-perovskite in the deep lower mantle, *Geophysical Journal International*, *197*(2), 910–919.

Dorfman, S. M., V. B. Prakapenka, Y. Meng, and T. S. Duffy (2012), Intercomparison of pressure standards (Au, Pt, Mo, MgO, NaCl and Ne) to 2.5 Mbar, *J. Geophys. Res.*, *117*(B8), n/a–n/a.

Dorfman, S. M., Y. Meng, V. B. Prakapenka, and T. S. Duffy (2013), Effects of Fe-enrichment on the equation of state and stability of (Mg,Fe)SiO3 perovskite, *Earth and Planetary Science Letters*, *361*(0), 249–257.

Dziewonski, A. M., and D. L. Anderson (1981), Preliminary reference Earth model, *Physics of the Earth and Planetary Interiors*, *25*(4), 297–356.

Fei, Y. (1999), Effects of temperature and composition on the bulk modulus of (Mg,Fe)O, *American Mineralogist*, *84*(3), 272–276.

Fiquet, G., D. Andrault, A. Dewaele, T. Charpin, M. Kunz, and D. Haüsermann (1998), P-V-T equation of state of MgSiO3 perovskite, *Physics of the Earth and Planetary Interiors*, *105*(1-2), 21–31.

Fiquet, G., A. Dewaele, D. Andrault, M. Kunz, and T. Le Bihan (2000), Thermoelastic Properties and Crystal Structure of MgSiO3 Perovskite at Lower Mantle Pressure and Temperature Conditions, *Geophys. Res. Lett.*, *27*, –.

Frost, D. J., C. Liebske, F. Langenhorst, C. A. McCammon, R. G. Tronnes, and D. C. Rubie (2004), Experimental evidence for the existence of iron-rich metal in the Earth's lower mantle, *Nature*, *428*(6981), 409–412.

Funamori, N., T. Yagi, W. Utsumi, T. Kondo, T. Uchida, and M. Funamori (1996), Thermoelastic properties of MgSiO3 perovskite determined by in situ X ray observations up to 30 GPa and 2000 K, *J. Geophys. Res.*, *101*(B4), 8257–8269.

Garnero, E. J., and A. K. McNamara (2008), Structure and Dynamics of Earth's Lower Mantle, *Science*, *320*(5876), 626–628.

Gillet, P., F. Guyot, and Y. Wang (1996), Microscopic anharmonicity and equation of state of MgSiO3-perovskite, *Geophys. Res. Lett.*, *23*(21), 3043–3046.

Glazyrin, K., T. Boffa Ballaran, D. Frost, C. McCammon, A. Kantor, M. Merlini, M. Hanfland, and L. Dubrovinsky (2014), Magnesium silicate perovskite and effect of iron oxidation state on its bulk sound velocity at the conditions of the lower mantle, *Earth and Planetary Science Letters*, *393*(0), 182–186.

Hammersley, A. P., S. O. Svensson, M. Hanfland, A. N. Fitch, and D. Hausermann (1996), Two-dimensional detector software: From real detector to idealised image or two-theta scan, *High Pressure Research*, *14*(4), 235–248.

Heinz, D. L., and R. Jeanloz (1987), Temperature measurements in the laser-heated diamond cell, in *Geophys. Monogr. Ser.*, vol. 39, pp. 113–127, AGU, Washington, DC.

Hernlund, J. W., and C. Houser (2008), On the statistical distribution of seismic velocities in Earth's deep mantle, *Earth and Planetary Science Letters*, *265*(3-4), 423–437.

Hinrichsen, B. (2006), Advances in data reduction of high-pressure x-ray powder diffraction data from two-dimensional detectors: a case study of schafarzikite (FeSb2O4).

Hinrichsen, B., R. E. Dinnebier, and M. Jansen (2008), Chapter 14 Two-dimensional Diffraction Using Area Detectors, in *Powder Diffraction: Theory and Practice*, pp. 414–438, The Royal Society of Chemistry.

Holzapfel, C., D. C. Rubie, D. J. Frost, and F. Langenhorst (2005), Fe-Mg Interdiffusion in (Mg,Fe)SiO3 Perovskite and Lower Mantle Reequilibration, *Science*, *309*(5741), 1707–1710.

Hsu, H., K. Umemoto, P. Blaha, and R. M. Wentzcovitch (2010a), Spin states and hyperfine interactions of iron in (Mg,Fe)SiO3 perovskite under pressure, *Earth and Planetary Science Letters*, *294*(1-2), 19–26, doi:10.1016/j.epsl.2010.02.031.

1147 Hsu, H., K. Umemoto, Z. Wu, and R. M. Wentzcovitch (2010b), Spin-State Crossover of
1148 Iron in Lower-Mantle Minerals: Results of DFT+U Investigations, *Reviews in Miner-*
1149 *alogy and Geochemistry*, *71*(1), 169–199, doi:10.2138/rmg.2010.71.09.

1150 Hsu, H., K. Umemoto, M. Cococcioni, and R. M. Wentzcovitch (2011), The Hub-
1151 bard U correction for iron-bearing minerals: A discussion based on (Mg,Fe)SiO3
1152 perovskite, *Physics of the Earth and Planetary Interiors*, *185*(1-2), 13–19, doi:
1153 10.1016/j.pepi.2010.12.001.

1154 Iizuka, R., H. Kagi, and K. Komatsu (2010), Comparing ruby fluorescence spectra at high
1155 pressure in between methanol-ethanol pressure transmitting medium and its deuteride,
1156 *Journal of Physics: Conference Series*, *215*(1), 012,177–.

1157 Irifune, T. (1994), Absence of an aluminous phase in the upper part of the Earth's lower-
1158 mantle, *Nature*, *370*(6485), 131–133.

1159 Irifune, T., T. Shinmei, C. A. McCammon, N. Miyajima, D. C. Rubie, and D. J. Frost
1160 (2010), Iron Partitioning and Density Changes of Pyrolite in Earth's Lower Mantle,
1161 *Science*, *327*(5962), 193–195.

1162 Ishii, M., and J. Tromp (1999), Normal-Mode and Free-Air Gravity Constraints on Lateral
1163 Variations in Velocity and Density of Earth's Mantle, *Science*, *285*(5431), 1231–1236,
1164 doi:10.1126/science.285.5431.1231.

1165 Jackson, J. M., J. Zhang, and J. D. Bass (2004), Sound velocities and elasticity of alu-
1166 minous MgSiO3 perovskite: Implications for aluminum heterogeneity in Earth's lower
1167 mantle, *Geophys. Res. Lett.*, *31*(10), L10,614–.

1168 Jackson, J. M., W. Sturhahn, G. Shen, J. Zhao, M. Y. Hu, D. Errandonea, J. D. Bass, and
1169 Y. Fei (2005), A synchrotron Mossbauer spectroscopy study of (Mg,Fe)SiO3 perovskite

1170 up to 120 GPa, *American Mineralogist*, *90*(1), 199–205.

1171 Jackson, J. M., W. Sturhahn, O. Tschauner, M. Lerche, and Y. Fei (2009), Behavior
1172 of iron in (Mg,Fe)SiO3 post-perovskite assemblages at Mbar pressures, *Geophys. Res.*
1173 *Lett.*, *36*, –.

1174 Jacobsen, S. D., C. M. Holl, K. A. Adams, R. A. Fischer, E. S. Martin, C. R. Bina, J.-F.
1175 Lin, V. B. Prakapenka, A. Kubo, and P. Dera (2008), Compression of single-crystal
1176 magnesium oxide to 118 GPa and a ruby pressure gauge for helium pressure media,
1177 *American Mineralogist*, *93*(11-12), 1823–1828, doi:10.2138/am.2008.2988.

1178 Katsura, T., S. Yokoshi, K. Kawabe, A. Shatskiy, M. A. G. M. Manthilake, S. Zhai,
1179 H. Fukui, H. A. C. I. Hegoda, T. Yoshino, D. Yamazaki, T. Matsuzaki, A. Yoneda,
1180 E. Ito, M. Sugita, N. Tomioka, K. Hagiya, A. Nozawa, and K.-i. Funakoshi (2009),
1181 P-V-T relations of MgSiO3 perovskite determined by in situ X-ray diffraction using a
1182 large-volume high-pressure apparatus, *Geophys. Res. Lett.*, *36*, –.

1183 Kesson, S. E., J. D. Fitz Gerald, and J. M. Shelley (1998), Mineralogy and dynamics of
1184 a pyrolite lower mantle, *Nature*, *393*(6682), 252–255.

1185 Kiefer, B., L. Stixrude, and R. M. Wentzcovitch (2002), Elasticity of (Mg,Fe)SiO3-
1186 perovskite at high pressures, *Geophys. Res. Lett.*, *29*(11), 34–1–34–4.

1187 Knittle, E., R. Jeanloz, and G. L. Smith (1986), Thermal expansion of silicate perovskite
1188 and stratification of the Earth's mantle.

1189 Kudoh, Y., C. T. Prewitt, L. W. Finger, A. Darovskikh, and E. Ito (1990), Effect of
1190 iron on the crystal structure of (Mg,Fe)SiO3 perovskite, *Geophys. Res. Lett.*, *17*(10),
1191 1481–1484.

1192 Lekic, V., S. Cottaar, A. Dziewonski, and B. Romanowicz (2012), Cluster analysis of
1193 global lower mantle tomography: A new class of structure and implications for chemical
1194 heterogeneity, *Earth and Planetary Science Letters*, *357-358*(0), 68–77.

1195 Li, B., and J. Zhang (2005), Pressure and temperature dependence of elastic wave velocity
1196 of MgSiO3 perovskite and the composition of the lower mantle, *Physics of the Earth*
1197 *and Planetary Interiors*, *151*(1-2), 143–154.

1198 Li, J., W. Sturhahn, J. Jackson, V. Struzhkin, J. Lin, J. Zhao, H. Mao, and G. Shen (2006),
1199 Pressure effect on the electronic structure of iron in (Mg,Fe)(Si,Al)O3 perovskite: a
1200 combined synchrotron Mössbauer and X-ray emission spectroscopy study up to 100
1201 GPa, *33*(8-9), 575–585–.

1202 Lu, R., A. M. Hofmeister, and Y. Wang (1994), Thermodynamic properties of ferromag-
1203 nesium silicate perovskites from vibrational spectroscopy, *J. Geophys. Res.*, *99*(B6),
1204 11,795–11,804.

1205 Lundin, S., K. Catalli, J. Santillán, S.-H. Shim, V. Prakapenka, M. Kunz, and Y. Meng
1206 (2008), Effect of Fe on the equation of state of mantle silicate perovskite over 1 Mbar,
1207 *Physics of the Earth and Planetary Interiors*, *168*, 97–102.

1208 Mao, H. K., R. J. Hemley, Y. Fei, J. F. Shu, L. C. Chen, A. P. Jephcoat, Y. Wu, and W. A.
1209 Bassett (1991), Effect of pressure, temperature, and composition on lattice parameters
1210 and density of (Fe,Mg)SiO3-perovskites to 30 GPa, *J. Geophys. Res.*, *96*(B5), 8069–
1211 8079.

1212 Mao, Z., J. Lin, H. Scott, H. Watson, V. Prakapenka, Y. Xiao, P. Chow, and C. Mc-
1213 Cammon (2011), Iron-rich perovskite in the Earth's lower mantle, *Earth and Planetary*
1214 *Science Letters*, *309*(3-4), 179–184, doi:10.1016/j.epsl.2011.06.030.

Mattern, E., J. Matas, Y. Ricard, and J. Bass (2005), Lower mantle composition and temperature from mineral physics and thermodynamic modelling, *Geophysical Journal International*, *160*(3), 973–990.

McCammon, C., I. Kantor, O. Narygina, J. Rouquette, U. Ponkratz, I. Sergueev, M. Mezouar, V. Prakapenka, and L. Dubrovinsky (2008), Stable intermediate-spin ferrous iron in lower-mantle perovskite, *Nature Geosci*, *1*(10), 684–687.

McNamara, A. K., and S. Zhong (2005), Thermochemical structures beneath Africa and the Pacific Ocean, *Nature*, *437*(7062), 1136–1139.

Metsue, A., and T. Tsuchiya (2012), Thermodynamic properties of (Mg,Fe2+)SiO3 perovskite at the lower-mantle pressures and temperatures: an internally consistent LSDA+U study, *Geophysical Journal International*, *190*(1), 310–322.

Murakami, M., Y. Ohishi, N. Hirao, and K. Hirose (2012), A perovskitic lower mantle inferred from high-pressure, high-temperature sound velocity data, *Nature*, *485*(7396), 90–94.

Ni, S., and D. V. Helmberger (2003), Seismological constraints on the South African superplume; could be the oldest distinct structure on earth, *Earth and Planetary Science Letters*, *206*(1-2), 119–131.

Ni, S., E. Tan, M. Gurnis, and D. Helmberger (2002), Sharp Sides to the African Superplume, *Science*, *296*(5574), 1850–1852.

O'Keeffe, M., B. Hyde, and J.-O. Bovin (1979), Contribution to the crystal chemistry of orthorhombic perovskites: MgSiO3 and NaMgF3, *4*(4), 299–305–.

Prakapenka, V. B., A. Kubo, A. Kuznetsov, A. Laskin, O. Shkurikhin, P. Dera, M. L. Rivers, and S. R. Sutton (2008), Advanced flat top laser heating system for high pressure

research at GSECARS: application to the melting behavior of germanium, *High Pressure Research*, *28*(3), 225–235, doi:10.1080/08957950802050718.

Ritsema, J., S. Ni, D. V. Helmberger, and H. P. Crotwell (1998), Evidence for strong shear velocity reductions and velocity gradients in the lower mantle beneath Africa, *Geophys. Res. Lett.*, *25*(23), 4245–4248.

Rivers, M., V. B. Prakapenka, A. Kubo, C. Pullins, C. M. Holl, and S. D. Jacobsen (2008), The COMPRES/GSECARS gas-loading system for diamond anvil cells at the Advanced Photon Source, *High Pressure Research*, *28*(3), 273–292, doi: 10.1080/08957950802333593.

Ross, N., and R. Hazen (1989), Single crystal X-ray diffraction study of MgSiO3 perovskite from 77 to 400 K, *16*(5), 415–420–.

Schuberth, B. S. A., H.-P. Bunge, G. Steinle-Neumann, C. Moder, and J. Oeser (2009), Thermal versus elastic heterogeneity in high-resolution mantle circulation models with pyrolite composition: High plume excess temperatures in the lowermost mantle, *Geochem. Geophys. Geosyst.*, *10*(1), Q01W01–.

Shen, G., M. L. Rivers, Y. Wang, and S. Sutton (2001), Laser heated diamond cell system at the Advanced Photon Source for in situ x-ray measurements at high pressure and temperature, *Review of Scientific Instruments*, *72*(2), 1273–1282.

Silvera, I. F., A. D. Chijioke, W. J. Nellis, A. Soldatov, and J. Tempere (2007), Calibration of the ruby pressure scale to 150 GPa, *physica status solidi (b)*, *244*(1), 460–467.

Sinmyo, R., E. Bykova, C. McCammon, I. Kupenko, V. Potapkin, and L. Dubrovinsky (2014), Crystal chemistry of Fe3+-bearing (Mg, Fe)SiO3 perovskite: a single-crystal X-ray diffraction study, *41*(6), 409–417–.

Sinogeikin, S. V., J. Zhang, and J. D. Bass (2004), Elasticity of single crystal and polycrystalline MgSiO3 perovskite by Brillouin spectroscopy, *Geophys. Res. Lett.*, *31*(6), L06,620–.

Sivia, D., and J. Skilling (2006), Data analysis: a Bayesian tutorial.

Steinberger, B., and T. H. Torsvik (2012), A geodynamic model of plumes from the margins of Large Low Shear Velocity Provinces, *Geochem. Geophys. Geosyst.*, *13*(1), Q01W09–.

Stixrude, L., and C. Lithgow-Bertelloni (2007), Influence of phase transformations on lateral heterogeneity and dynamics in Earth's mantle, *Earth and Planetary Science Letters*, *263*(1-2), 45–55.

Stixrude, L., and C. Lithgow-Bertelloni (2011), Thermodynamics of mantle minerals - II. Phase equilibria, *Geophysical Journal International*, *184*(3), 1180–1213.

Stixrude, L., R. J. Hemley, Y. Fei, and H. K. Mao (1992), Thermoelasticity of Silicate Perovskite and Magnesiowüstite and Stratification of the Earth's Mantle, *Science*, *257*(5073), 1099–1101.

Stixrude, L., N. de Koker, N. Sun, M. Mookherjee, and B. B. Karki (2009), Thermodynamics of silicate liquids in the deep Earth, *Earth and Planetary Science Letters*, *278*(3-4), 226–232.

Sturhahn, W. (2000), CONUSS and PHOENIX: Evaluation of nuclear resonant scattering data, *125*(1-4), 149–172–.

Sturhahn, W. (2004), Nuclear resonant spectroscopy, *Journal of Physics: Condensed Matter*, *16*(5), S497–.

Sturhahn, W., and J. M. Jackson (2007), Geophysical applications of nuclear resonant spectroscopy, *Geological Society of America Special Papers*, *421*, 157–174.

Sugahara, M., A. Yoshiasa, Y. Komatsu, T. Yamanaka, N. Bolfan-Casanova, A. Nakatsuka, S. Sasaki, and M. Tanaka (2006), Reinvestigation of the MgSiO3 perovskite structure at high pressure, *American Mineralogist*, *91*(4), 533–536, doi: 10.2138/am.2006.1980.

Sun, D., E. Tan, D. Helmberger, and M. Gurnis (2007), Seismological support for the metastable superplume model, sharp features, and phase changes within the lower mantle, *Proceedings of the National Academy of Sciences*, *104*(22), 9151–9155.

Sun, D., D. Helmberger, and M. Gurnis (2010), A narrow, mid-mantle plume below southern Africa, *Geophys. Res. Lett.*, *37*(9), L09,302–.

Tackley, P. J. (2011), Dynamics and evolution of the deep mantle resulting from thermal, chemical, phase and melting effects, *Earth-Science Reviews*, (0), –, doi: 10.1016/j.earscirev.2011.10.001.

Takemura, K. (2007), Pressure scales and hydrostaticity, *High Pressure Research: An International Journal*, *27*(4), 465–472.

Tan, E., and M. Gurnis (2005), Metastable superplumes and mantle compressibility, *Geophys. Res. Lett.*, *32*, –.

Tan, E., and M. Gurnis (2007), Compressible thermochemical convection and application to lower mantle structures, *J. Geophys. Res.*, *112*, –.

Tange, Y., Y. Nishihara, and T. Tsuchiya (2009a), Unified analyses for P-V-T equation of state of MgO: A solution for pressure-scale problems in high P-T experiments, *J. Geophys. Res.*, *114*(B3), B03,208–.

Tange, Y., E. Takahashi, Y. Nishihara, K.-i. Funakoshi, and N. Sata (2009b), Phase relations in the system MgO-FeO-SiO2 to 50 GPa and 2000°C: An application of experimental techniques using multianvil apparatus with sintered diamond anvils, *J. Geophys. Res.*, *114*(B2), B02,214–.

Tange, Y., Y. Kuwayama, T. Irifune, K.-i. Funakoshi, and Y. Ohishi (2012), P-V-T equation of state of MgSiO3 perovskite based on the MgO pressure scale: A comprehensive reference for mineralogy of the lower mantle, *J. Geophys. Res.*, *117*(B6), B06,201–.

Toby, B. (2001), EXPGUI, a graphical user interface for GSAS, *Journal of Applied Crystallography*, *34*(2), 210–213, doi:10.1107/S0021889801002242.

Toellner, T. (2000), Monochromatization of synchrotron radiation for nuclear resonant scattering experiments, *125*(1-4), 3–28–.

Torsvik, T. H., M. A. Smethurst, K. Burke, and B. Steinberger (2006), Large igneous provinces generated from the margins of the large low-velocity provinces in the deep mantle, *Geophysical Journal International*, *167*(3), 1447–1460.

Tschauner, O., C. Ma, J. R. Beckett, C. Prescher, V. B. Prakapenka, and G. R. Rossman (2014), Discovery of bridgmanite, the most abundant mineral in Earth, in a shocked meteorite, *Science*, *346*(6213), 1100–1102.

Vinet, P., J. Rose, J. Ferrante, and J. Smith (1989), Universal features of the equation of state of solids, *Journal of Physics: Condensed Matter*, *1*, 1941–1963.

Vinograd, V. L., and M. H. Sluiter (2006), Thermodynamics of mixing in pyrope-grossular, Mg3Al2Si3O12-Ca3Al2Si3O12, solid solution from lattice dynamics calculations and Monte Carlo simulations, *American Mineralogist*, *91*(11-12), 1815–1830.

Walter, M., A. Kubo, T. Yoshino, J. Brodholt, K. Koga, and Y. Ohishi (2004), Phase relations and equation-of-state of aluminous Mg-silicate perovskite and implications for Earth's lower mantle, *Earth and Planetary Science Letters*, *222*(2), 501–516.

Wang, Y., D. J. Weidner, R. C. Liebermann, and Y. Zhao (1994), P-V-T equation of state of (Mg,Fe)SiO3 perovskite: constraints on composition of the lower mantle, *Physics of The Earth and Planetary Interiors*, *83*(1), 13–40.

Wentzcovitch, R. M., B. B. Karki, M. Cococcioni, and S. de Gironcoli (2004), Thermoelastic Properties of $MgSiO_3$-Perovskite: Insights on the Nature of the Earth's Lower Mantle, *Phys. Rev. Lett.*, *92*(1), 018,501–.

You Shu-Jie, C. L.-C., and J. Chang-Qing (2009), Hydrostaticity of Pressure Media in Diamond Anvil Cells, *Chinese Physics Letters*, *26*(9), 096,202–.

Zhang, D., J. M. Jackson, W. Sturhahn, and Y. Xiao (2011), Local structure variations observed in orthoenstatite at high pressures, *American Mineralogist*, *96*(10), 1585–1592.

Zhang, L., Y. Meng, W. Yang, L. Wang, W. L. Mao, Q.-S. Zeng, J. S. Jeong, A. J. Wagner, K. A. Mkhoyan, W. Liu, R. Xu, and H.-k. Mao (2014), Disproportionation of (Mg,Fe)SiO3 perovskite in Earth's deep lower mantle, *Science*, *344*(6186), 877–882.

Figure 1. Sample X-ray diffraction patterns from high P-T experiments on 13% Fe-bearing bridgmanite sample, ranging between 33 and 120 GPa (at 300 K), using the *Dewaele et al.* [2008] Ne pressure scale. Diffraction peaks are color-coded as indicated in the legend, showing the bridgmanite sample (brg), neon (Ne), stishovite and post-stishovite silica phases (SiO_2), and the rhenium gasket (Re), along with uncertain gold peaks (Au?) and other unknown peaks (?). The upper panel displays 300 K example diffraction patterns, together with a laser-heated high P-T pattern in red, which are dominated by bridgmanite (cyan) and neon (red) peaks, with fitted peak positions indicated by ticks (*high-amplitude peaks are truncated for visibility*). To the right, the red-bordered panel shows a zoomed view of the bridgmanite-triplet and suggested H-phase region. For the high pressure pattern above ∼100 GPa, the red X's mark the expected positions of the unobserved H-phase 110 and 101 lines at 0.392 and 0.416 $\AA^{-1}$, respectively [*Zhang et al.*, 2014]. The central panel shows an interpolated cold-compression map of all unheated diffraction measurements, using a geometric intensity scale to make both high- and low-amplitude peaks visible. The lower panel displays the best-fit diffraction peak positions, showing the upward evolution of inverse d-spacing with compression for each diffraction line. The detailed panel to the right displays the H-phase and bridgmanite-triplet region, where the proposed H-phase peaks remain unobserved throughout the experiment.

Figure 2. Synchrotron Mössbauer spectroscopy time spectrum and associated power-spectrum (inset), collected for 13% Fe-bearing bridgmanite sample at P_{Ne} = 117 GPa and 300 K. The main panel shows the data as black circles with associated Poisson errorbars. The red solid and dashed lines represent the two best-fit CONUSS models described in the text. The solid line shows the preferred ferrous high-spin 2-site model, and the dashed line introduces an additional low quadrupole splitting site that contains ∼5% of the total iron in the high-spin ferric state, though this alternate model is statistically less likely.

Figure 3. Analysis of previous zero-pressure volume measurements of Al-free bridgmanite as a function of iron content. Error bars indicate uncertainty on diffraction measurements, which clearly under-predict the scatter between the measured samples. We model V_0 as linearly dependent on Fe composition, following *Kudoh et al.* [1990] and *Tange et al.* [2009b], together with an intrinsic scatter to represent the large sample-to-sample variation. The best-fit and 68% confidence intervals are shown in solid and dashed lines, and are used as priors in fitting both Fe-bearing and Fe-free datasets considered in this study.

Table 1. P-V-T Data for 13% Fe-bearing Bridgmanite

ID[a]	P [GPa]	$\sigma_{\Delta P}$ [GPa]	T [K]	V_{Pv} [Å^3]	V_{Ne} [Å^3]
1	33.15	0.65	300	146.59(24)	34.707(58)
1	33.88	0.58	300	145.81(21)	34.524(58)
1	37.95	0.84	300	144.97(30)	33.580(57)
1	39.50	0.86	300	144.32(30)	33.252(56)
1	41.91	0.42	300	142.88(11)	32.771(55)
1	44.58	0.68	300	142.23(21)	32.273(54)
1	46.85	0.73	300	141.49(22)	31.877(54)
1	49.21	0.92	300	140.53(28)	31.488(53)
1	51.39	0.73	300	139.52(20)	31.146(52)
1	55.20	1.39	300	138.53(41)	30.591(51)
1	56.22	0.90	300	138.40(25)	30.449(51)
1	59.22	1.03	300	137.40(28)	30.051(51)
1	61.07	1.19	300	137.14(33)	29.817(50)
1	63.17	0.82	300	136.23(20)	29.560(50)
1	64.21	0.88	300	136.06(22)	29.437(49)
1	66.38	0.81	300	135.48(19)	29.187(49)
1	67.88	0.80	300	135.01(18)	29.020(49)
1	70.84	1.02	300	134.08(24)	28.702(48)
1	73.92	1.11	300	133.38(26)	28.388(48)
1	73.39	0.94	300	133.72(21)	28.441(48)
1	74.57	0.79	300	133.07(16)	28.325(48)
1	74.95	0.96	300	133.17(21)	28.287(48)
1	76.94	0.94	300	132.38(20)	28.095(47)
1	79.58	1.17	300	131.90(26)	27.849(47)
1	81.59	1.01	300	131.26(21)	27.668(47)
1	85.09	1.04	300	130.65(21)	27.365(46)
1	86.34	0.97	300	130.44(19)	27.261(46)
1	86.64	1.35	300	130.22(29)	27.236(46)
1	87.62	0.98	300	130.39(19)	27.156(46)
1	88.87	1.07	300	129.88(21)	27.054(45)
1	90.14	1.38	300	129.25(28)	26.953(45)
1	92.68	1.00	300	128.59(18)	26.756(45)
1	93.20	1.11	300	128.68(21)	26.717(45)
1	95.41	1.17	300	128.33(22)	26.551(45)
1	96.95	0.99	300	127.91(17)	26.439(44)
1	98.72	1.54	300	127.56(30)	26.312(44)
1	103.54	1.61	300	125.99(30)	25.980(44)
1	104.68	1.12	300	126.31(19)	25.904(44)
1	106.09	1.26	300	126.37(22)	25.811(43)
1	109.67	2.10	300	125.12(39)	25.582(43)
1	111.20	1.31	300	124.55(22)	25.487(43)
1	111.03	0.96	300	125.39(13)	25.498(43)
1	112.88	1.33	300	124.61(22)	25.385(43)
1	114.60	2.02	300	123.89(36)	25.282(43)
1	108.59	1.97	300	124.91(36)	25.651(43)
1	113.88	1.79	300	124.96(32)	25.325(43)
1	116.98	1.78	300	124.19(31)	25.142(42)
1	120.09	2.08	300	122.42(35)	24.964(42)
1	117.19	1.30	300	124.52(21)	25.130(42)
2	43.88	1.27	1700(100)	146.35(48)	34.435(86)
2	44.32	1.32	1755(100)	146.38(50)	34.423(86)
2	49.71	1.85	1652(100)	142.58(63)	33.088(83)
2	48.88	1.84	1720(100)	142.49(62)	33.354(84)
2	50.43	1.73	1790(100)	142.63(58)	33.141(83)
2	49.40	1.58	1750(100)	142.64(53)	33.291(84)
2	49.46	1.61	1665(100)	142.69(54)	33.155(83)
2	50.83	1.28	1750(100)	143.50(43)	33.004(83)
2	54.21	0.77	1924(100)	142.52(22)	32.599(82)
2	61.32	1.40	1652(100)	140.14(42)	31.093(78)
2	62.38	1.51	1780(100)	140.21(46)	31.074(78)
2	64.86	2.39	1875(100)	139.70(74)	30.815(77)
2	62.20	1.37	1916(100)	139.20(40)	31.251(78)
2	63.78	1.46	2065(100)	139.24(43)	31.176(78)
2	71.07	1.65	1845(100)	136.88(45)	29.955(75)
2	71.16	1.71	1922(100)	136.93(47)	30.015(75)
2	71.66	1.50	2000(100)	136.90(40)	30.025(75)
2	71.51	1.56	2085(100)	137.29(42)	30.124(76)
2	71.73	1.34	1862(100)	136.63(34)	29.888(75)
2	72.18	1.36	1972(100)	136.60(35)	29.934(75)
2	72.95	1.33	2015(100)	136.68(34)	29.878(75)
2	84.76	1.61	2155(100)	133.71(38)	28.668(72)
2	83.17	1.67	1940(100)	133.63(39)	28.664(72)
2	84.01	1.29	1945(100)	133.80(28)	28.582(72)
2	84.64	1.28	1975(100)	133.79(28)	28.542(72)
2	85.84	1.24	2125(100)	133.92(27)	28.535(72)
2	87.81	1.24	2375(100)	133.96(27)	28.527(72)
2	84.19	1.28	1840(100)	133.81(28)	28.484(72)
2	83.70	1.23	1755(100)	133.86(26)	28.469(72)
2	84.00	1.31	1780(100)	133.91(29)	28.458(72)
2	83.53	0.96	1715(100)	133.56(17)	28.456(72)
2	84.12	1.36	1740(100)	133.71(30)	28.416(71)
2	84.12	1.57	1735(100)	133.75(37)	28.412(71)
2	84.59	1.32	1800(100)	133.84(29)	28.414(71)
2	85.02	1.35	1900(100)	133.82(30)	28.447(72)
2	85.91	1.36	2008(100)	133.89(30)	28.439(71)
2	95.37	1.74	1685(100)	130.59(36)	27.356(69)
2	94.28	1.92	1548(100)	130.63(41)	27.359(69)
2	95.61	1.57	1678(100)	130.74(32)	27.332(69)
2	94.38	1.65	1635(100)	130.21(34)	27.407(69)
2	95.31	1.68	1792(100)	130.25(34)	27.430(69)
2	95.55	1.58	1846(100)	130.36(32)	27.445(69)
2	95.85	1.94	1895(100)	130.24(41)	27.451(69)
2	96.14	2.01	1935(100)	130.47(43)	27.453(69)
2	96.70	1.79	2030(100)	130.69(38)	27.467(69)
2	103.11	1.45	1825(100)	128.73(26)	26.824(67)
2	102.52	1.53	1750(100)	128.70(28)	26.825(67)
2	102.30	1.36	1765(100)	128.99(23)	26.850(67)
2	102.47	1.59	1805(100)	128.92(30)	26.861(68)
2	102.34	1.60	1810(100)	128.90(30)	26.874(68)
2	102.51	1.76	1850(100)	128.95(34)	26.885(68)
2	102.65	1.47	1890(100)	128.94(27)	26.898(68)
2	102.88	1.44	1932(100)	128.93(26)	26.905(68)
2	113.71	2.28	1835(100)	126.27(42)	26.068(66)
2	112.72	1.26	1695(100)	126.34(16)	26.061(66)
2	113.24	1.78	1738(100)	126.52(31)	26.049(65)
2	112.47	1.70	1655(100)	126.56(29)	26.057(65)
2	112.70	2.17	1610(100)	126.45(40)	26.018(65)
2	112.83	1.75	1640(100)	126.53(30)	26.025(65)
2	113.35	1.69	1715(100)	126.56(29)	26.029(65)
2	113.67	1.74	1758(100)	126.56(30)	26.030(65)
2	112.90	1.49	1600(100)	126.26(23)	25.999(65)
2	113.51	1.81	1685(100)	126.47(32)	26.003(65)
2	114.61	1.49	1832(100)	126.45(23)	26.006(65)
2	114.66	1.44	1852(100)	126.54(22)	26.014(65)
2	114.91	1.86	1878(100)	126.54(33)	26.011(65)
2	114.66	2.30	1825(100)	126.34(43)	26.000(65)
2	118.63	1.69	2275(100)	126.58(28)	25.970(65)
2	117.69	1.77	2095(100)	126.61(31)	25.939(65)
2	123.71	2.03	2141(100)	124.77(34)	25.578(64)
2	120.30	1.39	1990(100)	125.39(19)	25.717(65)
2	119.76	1.44	1920(100)	125.40(20)	25.716(65)
2	119.65	1.38	1890(100)	125.40(19)	25.708(65)
2	120.48	1.40	2020(100)	125.42(19)	25.720(65)
2	121.20	1.41	2175(100)	125.41(20)	25.752(65)
2	121.55	1.39	2228(100)	125.42(19)	25.756(65)
2	121.48	1.39	2240(100)	125.40(19)	25.767(65)
2	126.59	2.37	2045(100)	124.05(40)	25.356(64)
2	126.34	2.58	2025(100)	124.42(45)	25.361(64)
2	125.71	2.58	1970(100)	123.98(45)	25.373(64)
2	121.37	1.98	1740(100)	124.96(33)	25.526(64)
2	122.26	2.14	1895(100)	124.55(36)	25.547(64)
2	122.61	2.33	1975(100)	124.33(40)	25.564(64)
2	123.11	1.65	2060(100)	124.94(25)	25.575(64)
2	123.63	1.77	2145(100)	125.14(28)	25.584(64)
2	123.63	2.43	2155(100)	125.23(44)	25.589(64)
2	123.96	1.75	2225(100)	125.22(28)	25.603(64)
2	124.14	2.86	2262(100)	124.54(52)	25.610(64)
2	123.80	2.19	2240(100)	124.55(37)	25.621(64)
2	126.03	2.30	2340(100)	124.82(40)	25.532(64)
2	122.33	2.62	1944(140)	124.52(47)	25.567(64)
2	121.06	2.29	1815(100)	124.63(40)	25.582(64)
2	120.89	4.20	1840(100)	124.19(78)	25.605(64)
2	128.72	1.78	1865(100)	122.98(26)	25.147(63)
2	129.18	2.21	1895(100)	124.32(37)	25.135(63)
2	130.08	3.36	1995(100)	124.89(62)	25.129(63)
2	130.73	2.54	1980(100)	124.90(45)	25.084(63)
2	127.35	1.46	2180(100)	124.60(19)	25.375(64)
2	127.72	1.69	2268(100)	124.68(26)	25.394(64)
2	128.35	1.79	2368(100)	124.69(28)	25.404(64)
2	128.62	1.71	2415(100)	124.70(26)	25.410(64)
2	128.67	1.79	2455(100)	124.56(28)	25.426(64)
2	132.27	2.58	1995(100)	124.81(45)	25.004(63)
2	132.70	3.76	2062(100)	124.59(70)	25.010(63)

Uncertainties are provided as appropriate for each quantity in parentheses (giving error in trailing digits).

These data are split into measurement groups with distinct measurement uncertainty characteristics, indicated by their ID value.

Temperature uncertainties are empirically estimated to be ∼100 K (except for one datum at ∼122 GPa, where the downstream measurement was unavailable, increasing error by $\sqrt{2}$).

[a] ID Key for DAC measurements: (1= 300 K, 2= Laser-Heated)

Table 2. P-V-T Data for Fe-free Bridgmanite (Reanalyzed from *Tange et al.* [2012])

ID[a]	P [GPa]	$\sigma_{\Delta P}$ [GPa]	T [K]	V_{Pv} [Å^3]	V_{MgO} [Å^3]	ID[a]	P [GPa]	$\sigma_{\Delta P}$ [GPa]	T [K]	V_{Pv} [Å^3]	V_{MgO} [Å^3]
1	30.43	0.17	1300	150.260(74)	66.4150(74)	3	59.98	0.21	1500(20)	139.930(22)	60.6300(329)
1	30.22	0.22	1100	149.630(94)	66.1360(67)	2	53.80	0.27	300	139.410(31)	60.3700(414)
1	29.67	0.23	900	149.130(94)	65.9500(47)	3	60.81	0.33	1980(30)	140.900(22)	61.0600(548)
1	28.97	0.25	700	148.770(100)	65.8100(134)	2	51.71	0.33	300	140.110(41)	60.7200(517)
1	28.68	0.17	500	148.420(67)	65.5860(74)	3	68.94	0.13	1500(20)	137.230(22)	59.2080(164)
1	27.96	0.10	300	148.260(40)	65.5060(13)	2	60.63	0.16	300	137.320(41)	59.2810(114)
1	42.82	0.16	1500	145.920(47)	63.8500(201)	3	93.64	0.46	1500(20)	131.150(99)	55.9200(219)
1	42.14	0.14	1300	145.600(47)	63.7100(134)	3	86.15	0.19	1900(30)	133.408(21)	57.2100(219)
1	41.37	0.41	1100	145.170(53)	63.5910(802)	3	83.92	0.19	1500(20)	133.270(22)	57.1200(219)
1	41.02	0.13	900	144.830(40)	63.3900(134)	2	76.10	1.59	300	133.280(31)	57.1000(2068)
1	40.33	0.15	700	144.500(53)	63.2660(74)	3	108.51	0.27	1870(60)	128.140(55)	54.5680(88)
1	39.67	0.14	500	144.280(47)	63.1510(74)	3	106.07	0.21	1550(50)	128.140(44)	54.5690(44)
1	39.02	0.18	300	144.140(53)	63.0700(201)	2	97.74	0.28	300	128.100(52)	54.5450(145)
1	52.30	0.12	1500	142.420(33)	61.9800(134)	3	104.21	0.16	2430(60)	130.040(33)	55.5050(77)
1	51.73	0.16	1300	142.130(47)	61.8310(127)	2	88.84	0.20	300	130.140(31)	55.5370(165)
1	51.14	0.16	1100	141.770(47)	61.6900(134)						
1	50.63	0.18	900	141.460(53)	61.5400(134)						
1	50.15	0.22	700	141.190(53)	61.3900(267)						
1	49.42	0.21	500	140.970(47)	61.3000(267)						
1	48.72	0.15	300	140.820(33)	61.2400(201)						
1	62.22	0.25	1500	139.330(74)	60.2600(134)						
1	62.56	0.27	1300	138.790(74)	59.9800(201)						
1	62.43	0.32	1100	138.450(60)	59.7800(401)						
1	61.82	0.36	900	138.130(87)	59.6600(334)						
1	61.51	0.49	700	137.800(127)	59.5000(334)						
1	60.91	0.45	500	137.570(114)	59.4000(334)						
1	60.58	0.43	300	137.380(107)	59.2900(334)						

Uncertainties are provided as appropriate for each quantity in parentheses (giving error in trailing digits).

These data are split into measurement groups with distinct measurement uncertainty characteristics, indicated by their ID value.

[a] ID Key for measurements: (1= Sintered Diamond Multi-Anvil, 2= 300 K DAC, 3=Laser-Heated DAC)

Table 3. Vinet and Mie-Grüneisen-Debye Equation of State Parameters for Bridgmanite

X_{Fe}	13% Fe [a]	0% Fe [b]
V_0 [$\mathring{A}^3$]	163.16(19)	162.12(13)
K_{0T} [GPa]	243.8(43)	262.3(32)
K'_{0T}	4.160(110)	4.044(75)
Θ_0 [K]	1000	1000
γ_0	1.400(110)	1.675(45)
q	0.56(37)	1.39(16)

We fix the zero-pressure Debye temperature to the value $\Theta_0 = 1000$ K, consistent with the best-fit value for the Fe-free dataset (see text for details).

Priors: $\gamma_0 = 1 \pm 1$, $q = 1 \pm 1$, and $V_0 = 163.2 \pm 0.2$ and 162.5 ± 0.2 $\mathring{A}^3$, for 13% and 0% Fe bridgmanite samples.

Error estimates give a 68% confidence interval.

[a] data from this work—uses Neon pressure scale from *Dewaele et al.* [2008]

[b] data reanalyzed from *Tange et al.* [2012]—uses MgO pressure scale from *Tange et al.* [2009a]

Figure 4. Fitted high P-T equations of state for 13% Fe-bearing bridgmanite and Fe-free bridgmanite shown in the upper and lower panels, respectively. The data are shown color-coded by temperature, with the reduced isothermal data shown with open circles comparing well to the dark blue 300 K isotherms, and the corresponding measured data represented by crosses. The data for the Fe-free $MgSiO_3$ sample is from *Tange et al.* [2012], but has been reanalyzed using **pvt-tool** to incorporate our new adjusted error model. The inset panels each show a histogram of the normalized pressure residuals, $(P_{mod} - P_{obs})/\sigma_P$, where the unheated and heated contributions are separately shown in blue and red, respectively, together with the total histogram in black. These residuals all compare favorably with a standard normal distribution, shown by the gray line, reflecting the effectiveness of our error-modeling approach.

Table 4. Equation of State Parameter Correlations

	$X_{\mathrm{Fe}} = 13\%$ [a]				
	V_0	K_{0T}	K'_{0T}	γ_0	q
V_0	+1.00	−0.85	+0.62	+0.03	+0.03
K_{0T}	−0.85	+1.00	−0.93	−0.32	−0.32
K'_{0T}	+0.62	−0.93	+1.00	+0.48	+0.50
γ_0	+0.03	−0.32	+0.48	+1.00	+0.97
q	+0.03	−0.32	+0.50	+0.97	+1.00
	$X_{\mathrm{Fe}} = 0\%$ [b]				
	V_0	K_{0T}	K'_{0T}	γ_0	q
V_0	+1.00	−0.96	+0.85	−0.12	−0.16
K_{0T}	−0.96	+1.00	−0.96	−0.07	−0.02
K'_{0T}	+0.85	−0.96	+1.00	+0.27	+0.24
γ_0	−0.12	−0.07	+0.27	+1.00	+0.95
q	−0.16	−0.02	+0.24	+0.95	+1.00

The correlation matrix ρ is a convenient scaled form of the covariance matrix $\mathbf{\Sigma}$, where the correlation coefficient between parameters i and j is simply: $\rho_{ij} = \frac{\Sigma_{ij}}{\sqrt{\Sigma_{ii}\Sigma_{jj}}}$.

a, b: See footnote to Table 3.

Figure 5. Normalized axial ratios and octahedral tilt angles are shown in the upper and lower panels for the 0% and 13% Fe-bearing bridgmanite samples. The 13% Fe sample measured in this study is plotted in red crosses while the Fe-free data from *Tange et al.* [2012] is shown in black circles. Best-fit linear trends are displayed as solid lines, and reflect the systematic effect of adding iron on bridgmanite's crystal geometry.

Figure 6. Covariance between the primary *cold* parameters (at 300 K) (K_{0T}, K'_{0T}), defining the room temperature isotherm, and the *thermal* parameters (γ_0, q), are shown in panels (a) and (b), respectively. These ellipses represent the 68% confidence regions for the 13% Fe-bearing bridgmanite sample in red and the Fe-free sample in black. Also shown in black crosses are the originally reported best-fit Fe-free values from *Tange et al.* [2012]. These parameter values are generally inconsistent with our analysis due to important differences in the fitting procedure, including the use of a prior on V_0 in place of fixing its value, in addition to our adjustment of the estimated observational errors to ensure consistency with the model residuals.

Figure 7. The derived equation of state models for 13% Fe-bearing and Fe-free bridgmanite are used to sample the 68% confidence bounds for a set of high P-T profiles relevant to the Earth's mantle. The Fe-bearing and Fe-free bridgmanite samples are represented using red and gray shaded regions, respectively. The upper panel shows the evolution of volume for a set of isothermal profiles, clearly depicting the reduced thermal expansion properties of Fe-bearing bridgmanite. The lower panel shows the density and adiabatic bulk modulus anomalies (relative to PREM) for a bridgmanite-only lower mantle; geotherm composed of a representative 1873 K mantle adiabat (defined at 670 km, *Brown and Shankland* 1981) and a thermal boundary layer rising to a CMB temperature of 4000 K. Despite the large differences in thermal properties, the adiabatic bulk moduli of these two compositions are quite similar, and are nearly indistinguishable throughout the bottom half of the lower mantle.

Table 5. Geothermal Profiles for 13%-Fe (Fe-free) Bridgmanite

P [GPa]	T [K]	ρ [g/cc]	K_S [GPa]	α [1e-5/K]	γ []	$C_V/(3Nk_B)$ []
23.8	1873 (1873)	4.47 (4.29)	318.2 (325.1)	2.38 (2.76)	1.36 (1.58)	0.9838 (0.9839)
26.1	1891 (1893)	4.50 (4.32)	326.6 (333.2)	2.33 (2.68)	1.36 (1.57)	0.9838 (0.9839)
28.4	1908 (1913)	4.53 (4.34)	334.9 (341.3)	2.27 (2.60)	1.35 (1.55)	0.9838 (0.9839)
30.6	1925 (1932)	4.56 (4.37)	343.2 (349.3)	2.22 (2.53)	1.35 (1.54)	0.9838 (0.9839)
32.9	1942 (1951)	4.59 (4.40)	351.4 (357.2)	2.18 (2.46)	1.34 (1.52)	0.9838 (0.9839)
35.1	1959 (1970)	4.62 (4.43)	359.6 (365.1)	2.13 (2.40)	1.34 (1.51)	0.9838 (0.9839)
37.4	1975 (1988)	4.65 (4.46)	367.7 (373.0)	2.09 (2.34)	1.33 (1.50)	0.9838 (0.9839)
39.7	1991 (2006)	4.68 (4.48)	375.8 (380.8)	2.05 (2.28)	1.33 (1.49)	0.9838 (0.9839)
41.9	2006 (2023)	4.71 (4.51)	383.8 (388.5)	2.01 (2.23)	1.32 (1.47)	0.9838 (0.9839)
44.2	2022 (2040)	4.74 (4.54)	391.8 (396.3)	1.97 (2.18)	1.32 (1.46)	0.9838 (0.9839)
46.5	2037 (2057)	4.76 (4.56)	399.7 (404.0)	1.94 (2.13)	1.32 (1.45)	0.9838 (0.9839)
48.7	2052 (2074)	4.79 (4.59)	407.6 (411.6)	1.90 (2.08)	1.31 (1.44)	0.9838 (0.9839)
51.0	2067 (2090)	4.82 (4.61)	415.4 (419.2)	1.87 (2.04)	1.31 (1.43)	0.9838 (0.9839)
53.2	2081 (2106)	4.84 (4.64)	423.2 (426.8)	1.84 (2.00)	1.30 (1.42)	0.9838 (0.9839)
55.5	2095 (2121)	4.87 (4.66)	431.0 (434.3)	1.81 (1.95)	1.30 (1.41)	0.9838 (0.9839)
57.8	2109 (2137)	4.89 (4.69)	438.7 (441.8)	1.78 (1.91)	1.30 (1.40)	0.9838 (0.9839)
60.0	2123 (2152)	4.92 (4.71)	446.4 (449.3)	1.75 (1.88)	1.29 (1.39)	0.9838 (0.9839)
62.3	2137 (2167)	4.94 (4.73)	454.0 (456.8)	1.72 (1.84)	1.29 (1.38)	0.9838 (0.9839)
64.5	2150 (2181)	4.97 (4.76)	461.6 (464.2)	1.70 (1.81)	1.28 (1.37)	0.9838 (0.9839)
66.8	2164 (2196)	4.99 (4.78)	469.2 (471.6)	1.67 (1.77)	1.28 (1.36)	0.9838 (0.9839)
69.1	2177 (2210)	5.02 (4.80)	476.8 (478.9)	1.65 (1.74)	1.28 (1.35)	0.9838 (0.9839)
71.3	2190 (2224)	5.04 (4.82)	484.3 (486.3)	1.63 (1.71)	1.27 (1.34)	0.9838 (0.9839)
73.6	2203 (2237)	5.06 (4.85)	491.8 (493.6)	1.61 (1.68)	1.27 (1.33)	0.9838 (0.9839)
75.9	2216 (2251)	5.09 (4.87)	499.2 (500.8)	1.58 (1.65)	1.27 (1.32)	0.9838 (0.9839)
78.1	2228 (2264)	5.11 (4.89)	506.7 (508.1)	1.56 (1.62)	1.26 (1.32)	0.9838 (0.9839)
80.4	2241 (2277)	5.13 (4.91)	514.1 (515.3)	1.54 (1.60)	1.26 (1.31)	0.9838 (0.9839)
82.6	2253 (2290)	5.15 (4.93)	521.4 (522.5)	1.52 (1.57)	1.26 (1.30)	0.9838 (0.9839)
84.9	2265 (2303)	5.18 (4.96)	528.8 (529.7)	1.50 (1.55)	1.26 (1.29)	0.9838 (0.9839)
87.2	2277 (2316)	5.20 (4.98)	536.1 (536.8)	1.49 (1.52)	1.25 (1.29)	0.9838 (0.9839)
89.4	2289 (2328)	5.22 (5.00)	543.4 (544.0)	1.47 (1.50)	1.25 (1.28)	0.9838 (0.9839)
91.7	2301 (2340)	5.24 (5.02)	550.7 (551.1)	1.45 (1.48)	1.25 (1.27)	0.9838 (0.9839)
94.0	2312 (2352)	5.26 (5.04)	557.9 (558.2)	1.43 (1.45)	1.24 (1.26)	0.9838 (0.9839)
96.2	2324 (2364)	5.28 (5.06)	565.2 (565.2)	1.42 (1.43)	1.24 (1.26)	0.9838 (0.9839)
97.3	2329 (2370)	5.29 (5.07)	568.8 (568.7)	1.41 (1.42)	1.24 (1.25)	0.9838 (0.9839)
99.6	2341 (2382)	5.32 (5.09)	575.9 (575.8)	1.39 (1.40)	1.24 (1.25)	0.9838 (0.9839)
101.9	2352 (2393)	5.34 (5.11)	583.1 (582.8)	1.38 (1.38)	1.23 (1.24)	0.9838 (0.9839)
104.1	2363 (2405)	5.36 (5.13)	590.3 (589.8)	1.36 (1.36)	1.23 (1.23)	0.9838 (0.9839)
106.4	2375 (2417)	5.38 (5.15)	597.4 (596.7)	1.35 (1.34)	1.23 (1.23)	0.9838 (0.9839)
108.7	2387 (2429)	5.40 (5.17)	604.5 (603.7)	1.34 (1.33)	1.23 (1.22)	0.9838 (0.9839)
110.9	2401 (2443)	5.42 (5.19)	611.5 (610.6)	1.32 (1.31)	1.22 (1.21)	0.9838 (0.9839)
113.2	2418 (2460)	5.44 (5.21)	618.5 (617.4)	1.31 (1.29)	1.22 (1.21)	0.9839 (0.9840)
115.4	2442 (2483)	5.46 (5.22)	625.4 (624.0)	1.30 (1.28)	1.22 (1.20)	0.9841 (0.9842)
117.7	2477 (2518)	5.47 (5.24)	632.1 (630.5)	1.29 (1.26)	1.22 (1.20)	0.9844 (0.9845)
120.0	2531 (2571)	5.49 (5.26)	638.6 (636.6)	1.28 (1.25)	1.22 (1.19)	0.9850 (0.9850)
122.2	2612 (2650)	5.50 (5.27)	644.8 (642.2)	1.27 (1.24)	1.21 (1.19)	0.9858 (0.9858)
124.5	2731 (2766)	5.52 (5.28)	650.5 (647.8)	1.26 (1.23)	1.21 (1.18)	0.9869 (0.9869)
126.8	2896 (2926)	5.53 (5.29)	655.6 (651.4)	1.26 (1.23)	1.21 (1.18)	0.9883 (0.9882)
129.0	3111 (3136)	5.53 (5.30)	660.2 (654.7)	1.25 (1.23)	1.21 (1.18)	0.9898 (0.9897)
131.3	3375 (3392)	5.53 (5.30)	664.2 (657.1)	1.25 (1.23)	1.21 (1.18)	0.9914 (0.9912)
133.5	3677 (3686)	5.53 (5.30)	667.8 (658.9)	1.25 (1.23)	1.21 (1.18)	0.9927 (0.9925)
135.8	4000 (4000)	5.53 (5.31)	671.1 (660.9)	1.25 (1.23)	1.21 (1.18)	0.9938 (0.9936)

Computed from equation of state parameters in Table 3 using *Brown and Shankland* [1981]

Figure 8. An ideal mixture model is used to sample the behavior of bridgmanite under a range of temperatures and compositions, corresponding to potential conditions for a bridgmanite-dominated lower-mantle region. Panel (a) depicts the nominal bulk mantle geotherm (in gray) with a potentially elevated thermal profile through a bridgmanite-dominate region (in red). The lower-mantle geotherm corresponds to the 1873 K mantle adiabat (at 670 km) from *Brown and Shankland* [1981] (gray dashed-line) combined with an additional thermal boundary layer up to the nominal CMB temperature of 4000 K. We consider elevated bridgmanite thermal profiles with excess temperatures of ΔT_{ex} above the reference adiabat (defined at 120 GPa), overlying an additional thermal boundary layer reaching the nominal core temperature. In Panel (b), a range of ΔT_{ex} and Fe-composition values are explored, where the behavior of bridgmanite is calculated from our ideal mixing model, and the results are mapped as percentage anomalies relative to PREM at 120 GPa, with density anomalies in solid contours and adiabatic bulk modulus anomalies in dashed contours. Bridgmanite's bulk modulus just outside the thermal boundary layer tends to be about 1% to 3% higher than the average mantle, while the density contrast depends strongly on composition. The zero-difference contours (in gray) never intersect, indicating that no combination of temperature and composition for pure bridgmanite is capable of reproducing average mantle properties.

Figure 9. Thermo-chemical pile hypotheses for bridgmanite-dominated LLSVPs are explored using our ideal mixing model. Panel (a) shows pile density anomalies (relative to PREM) assuming a nominal excess temperature of 900 K, using the adiabat plus thermal boundary layer construction of Figure 8. By considering a range of Fe-contents, we see a systematic shift in relative buoyancy changing from a dense stable layer above 13% Fe, that is everywhere denser except in the thermal boundary layer, through a neutrally-buoyant structure at 12% Fe with a density crossover near ∼70 GPa, to a fully unstable transient layer below 11% Fe. Panel (b) applies this relative buoyancy calculation for the plausible range of LLSVP temperatures [*Tackley*, 2011], to map out the different buoyancy regimes: The metastable dome region (shown in the narrow pink wedge) is defined by density crossover depths yielding 600 to 1200 km tall structures above the CMB, consistent with the observed LLSVPs; stable passive piles (to the right of the gray line) require dynamic stresses to lift these otherwise flat dense layers off the CMB; while dynamically unstable structures (shaded in green) readily escape through convection, erasing the chemically distinct reservoir. The probability of the metastable dome and stable passive pile hypotheses for LLSVPs is determined by the relative area of those regions that falls within plausible density anomaly limits [e.g. *Ishii and Tromp*, 1999], shown in solid colored contours. This metastable dome probability is only $\mathcal{P}\sim4\%$ if allowing up to 3% density anomalies, and rises to $\mathcal{P}\sim7\%$ if restricted to 1.5% density anomalies.

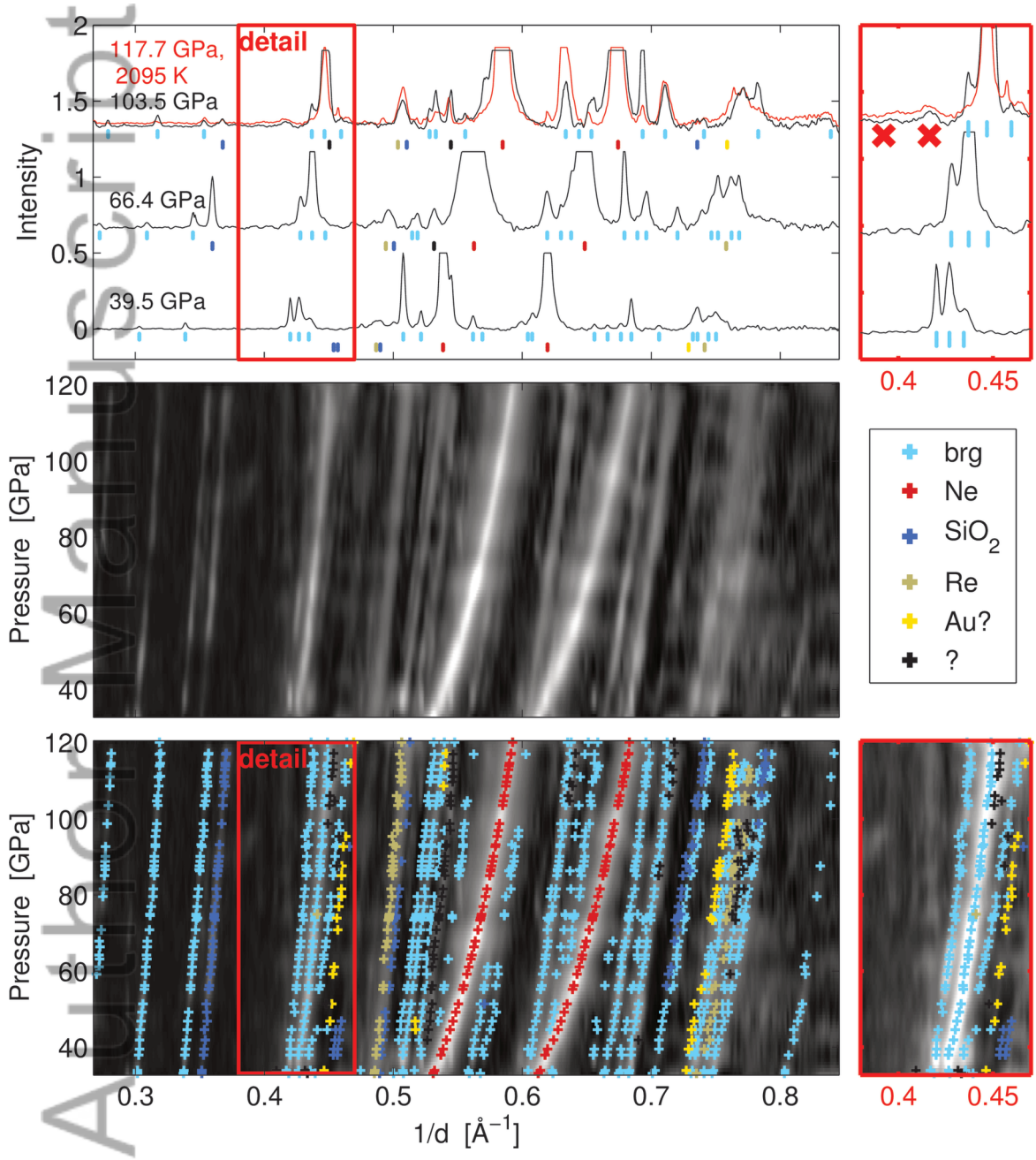

fig1

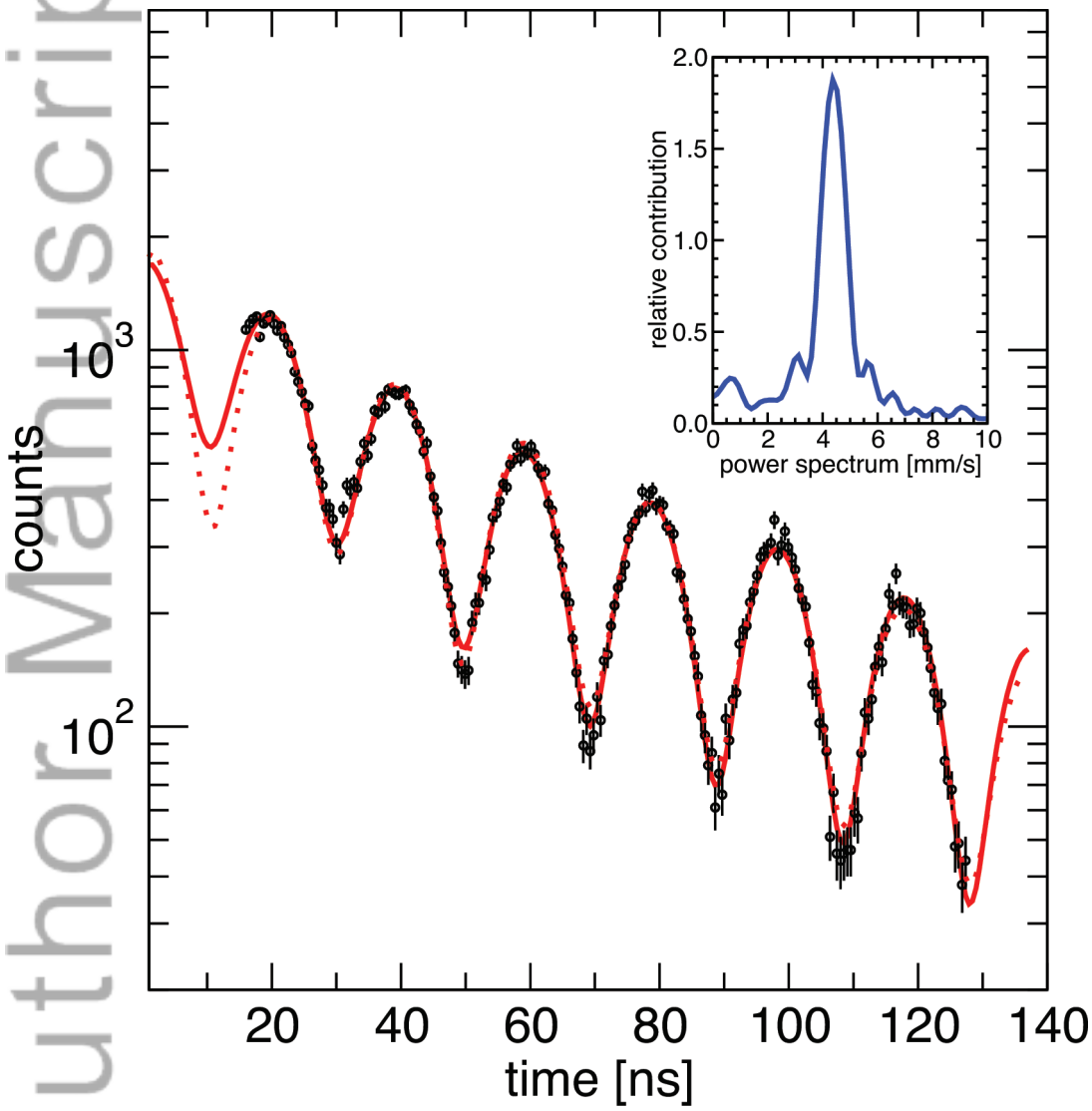

fig2

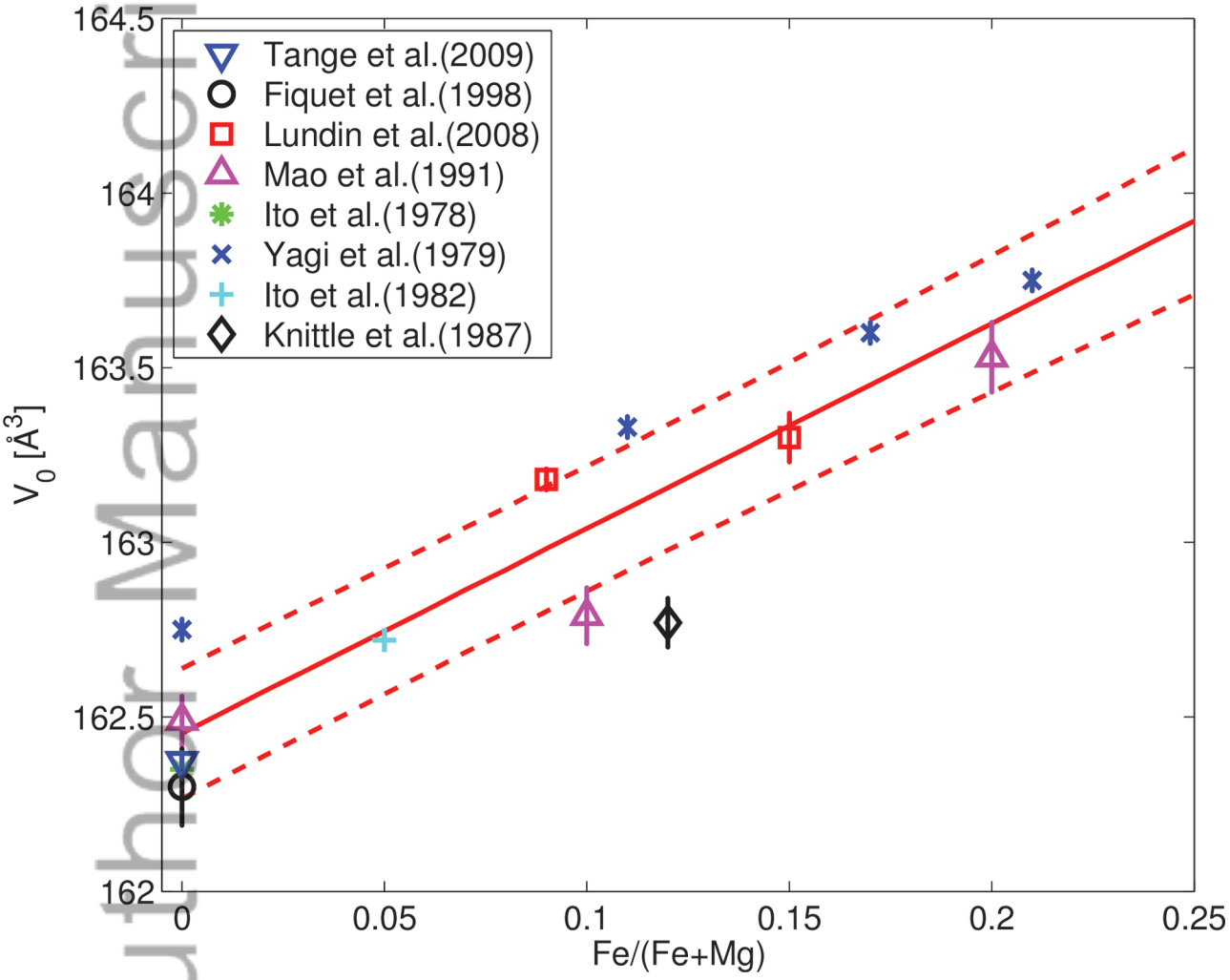

fig3

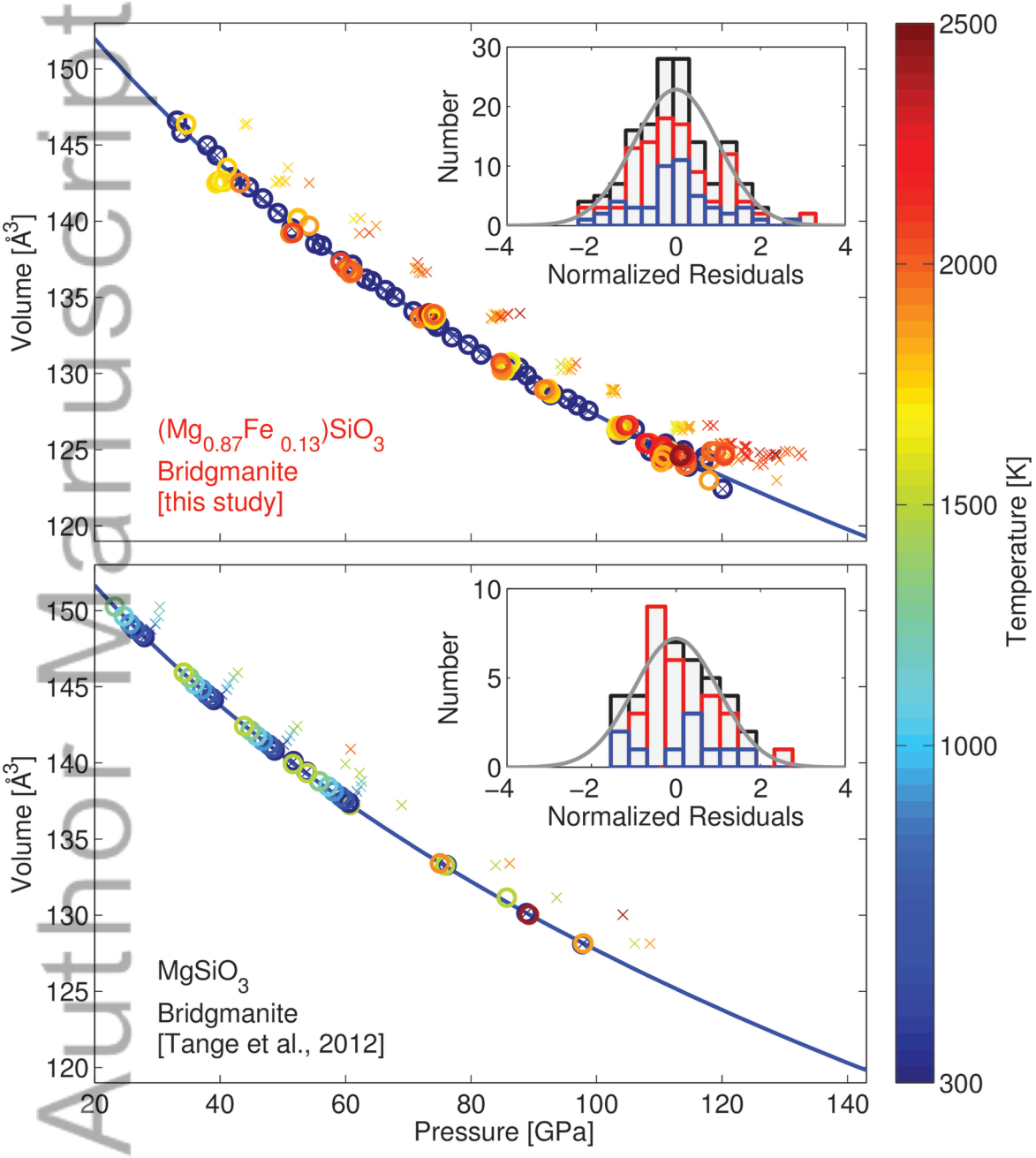

fig4

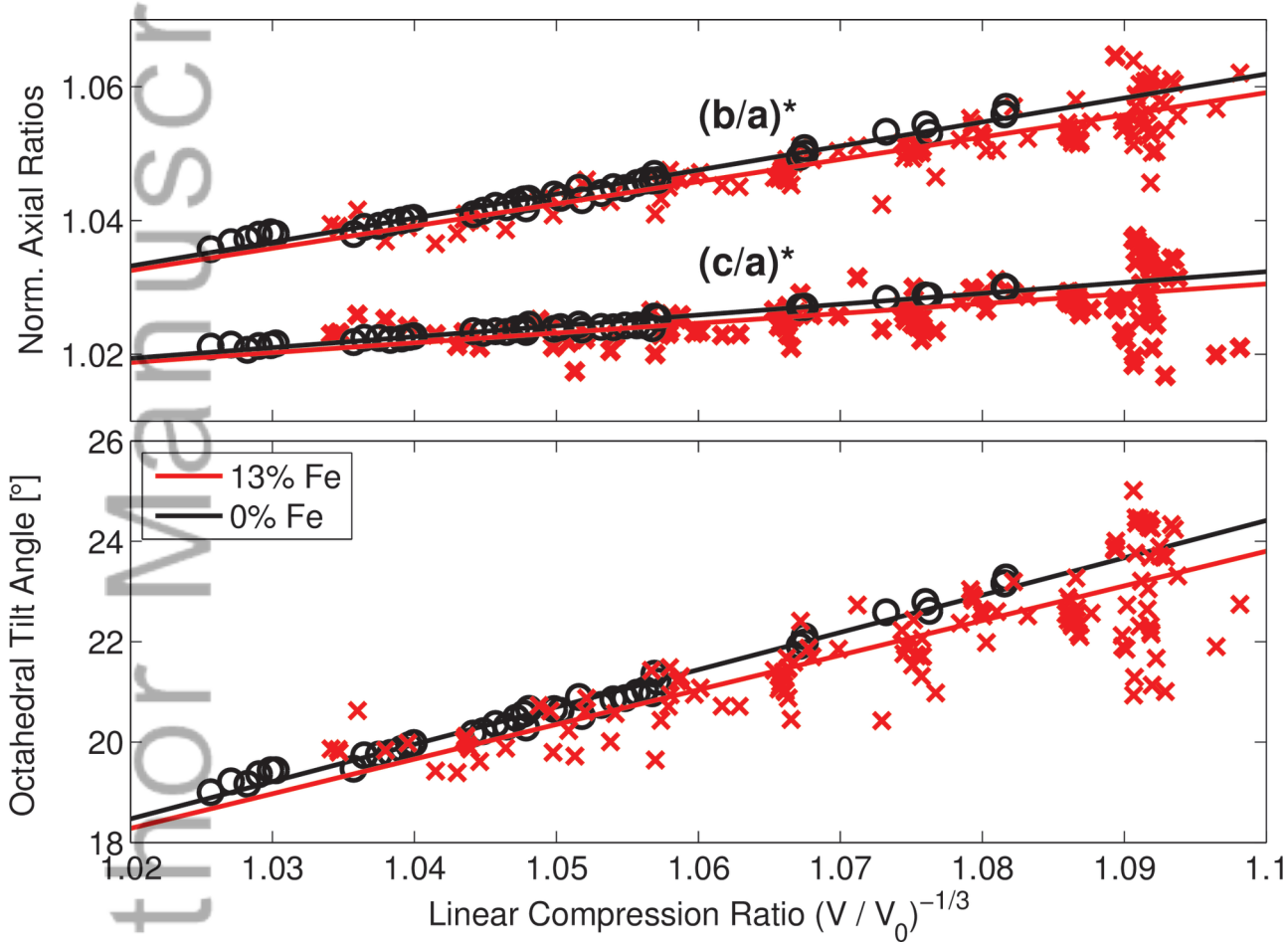

fig5

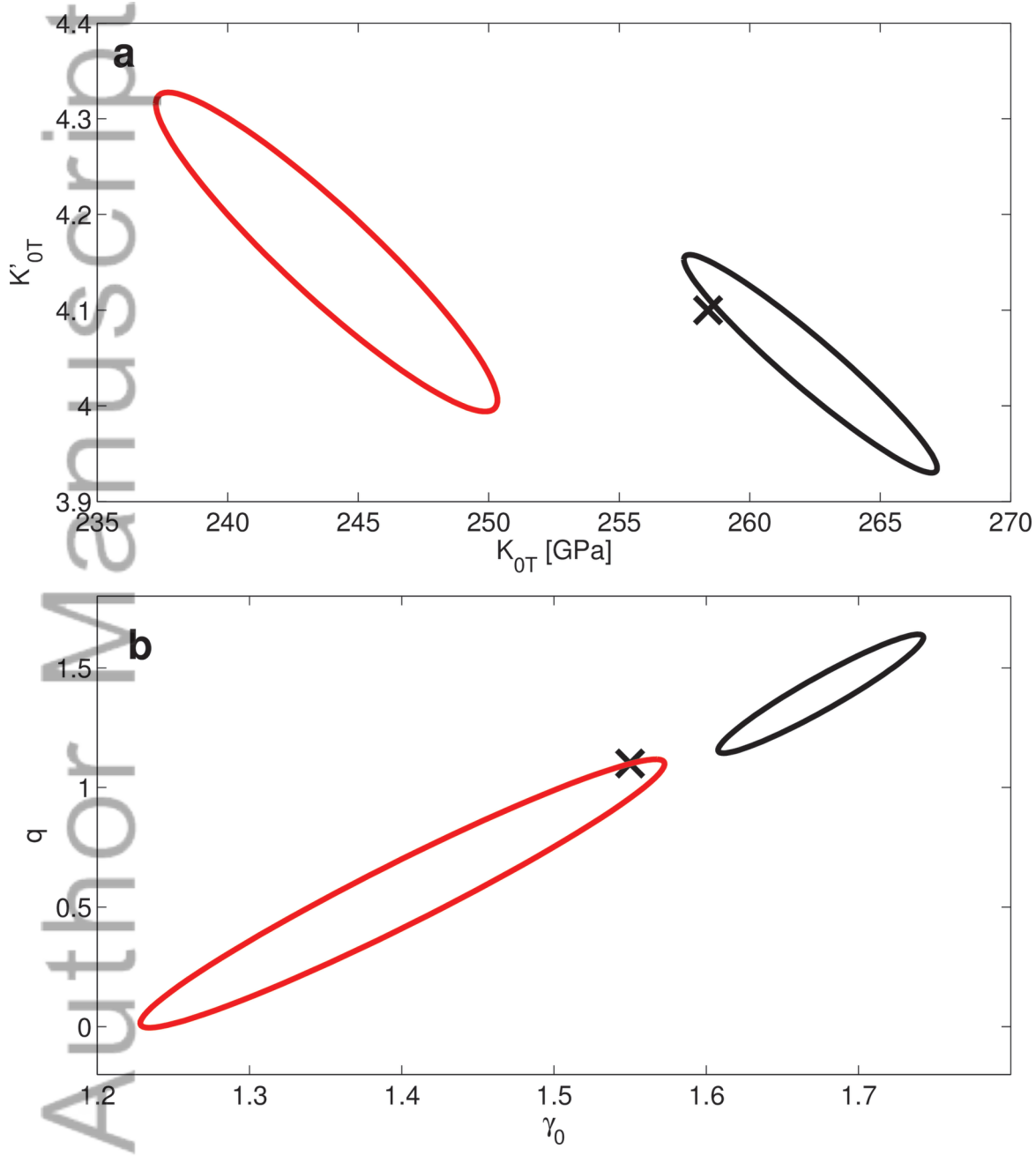

fig6

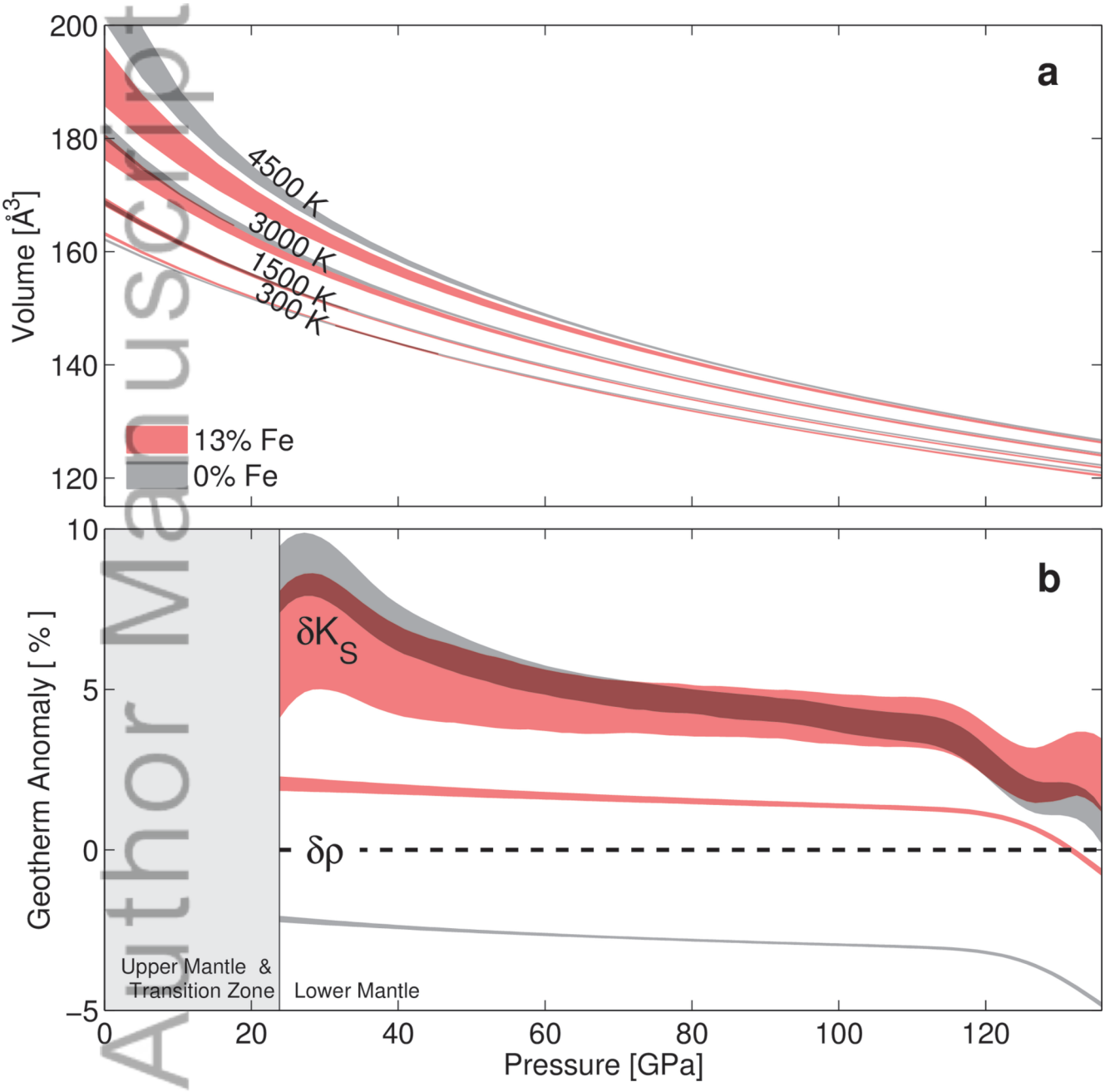

fig7

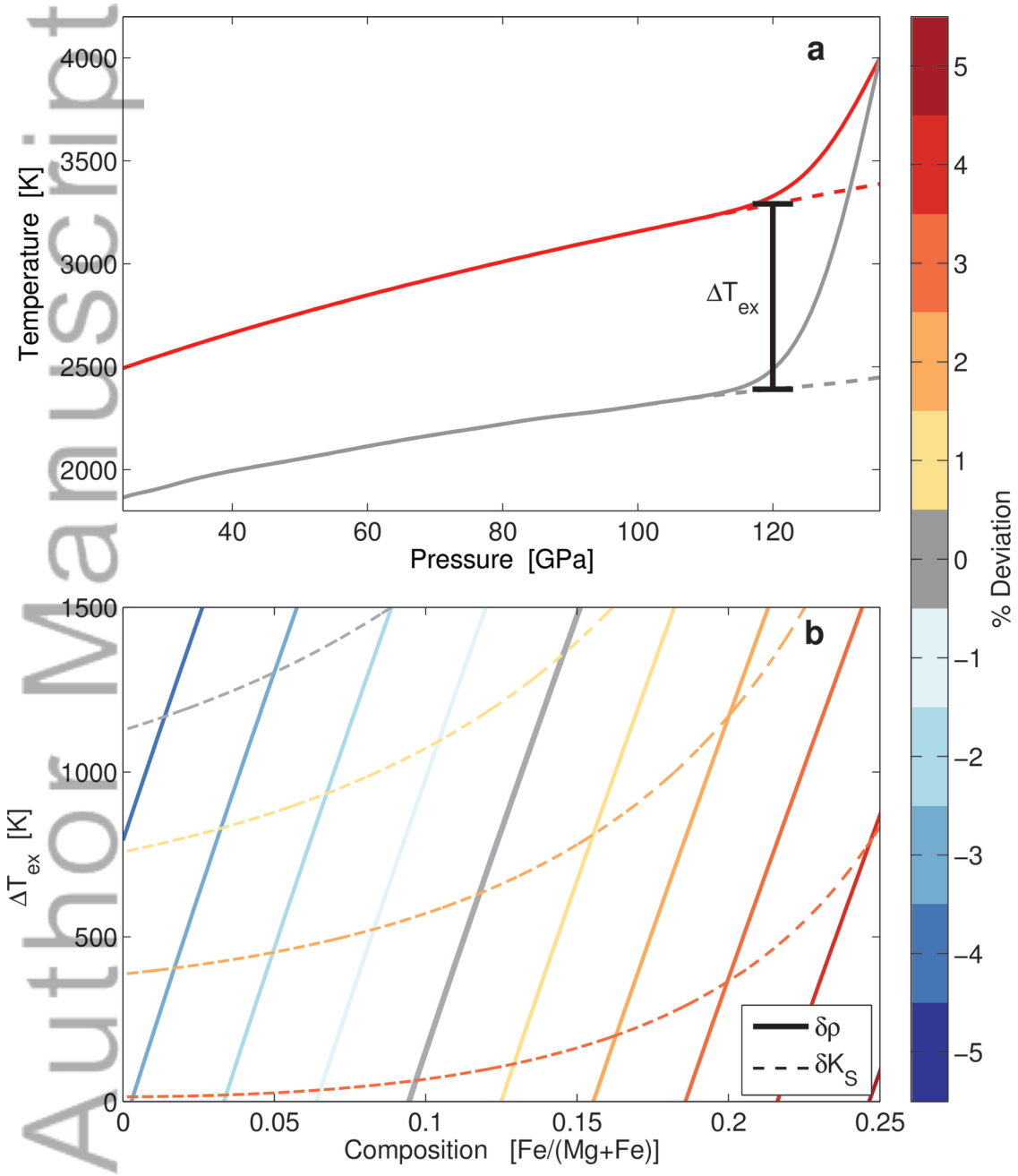

fig8

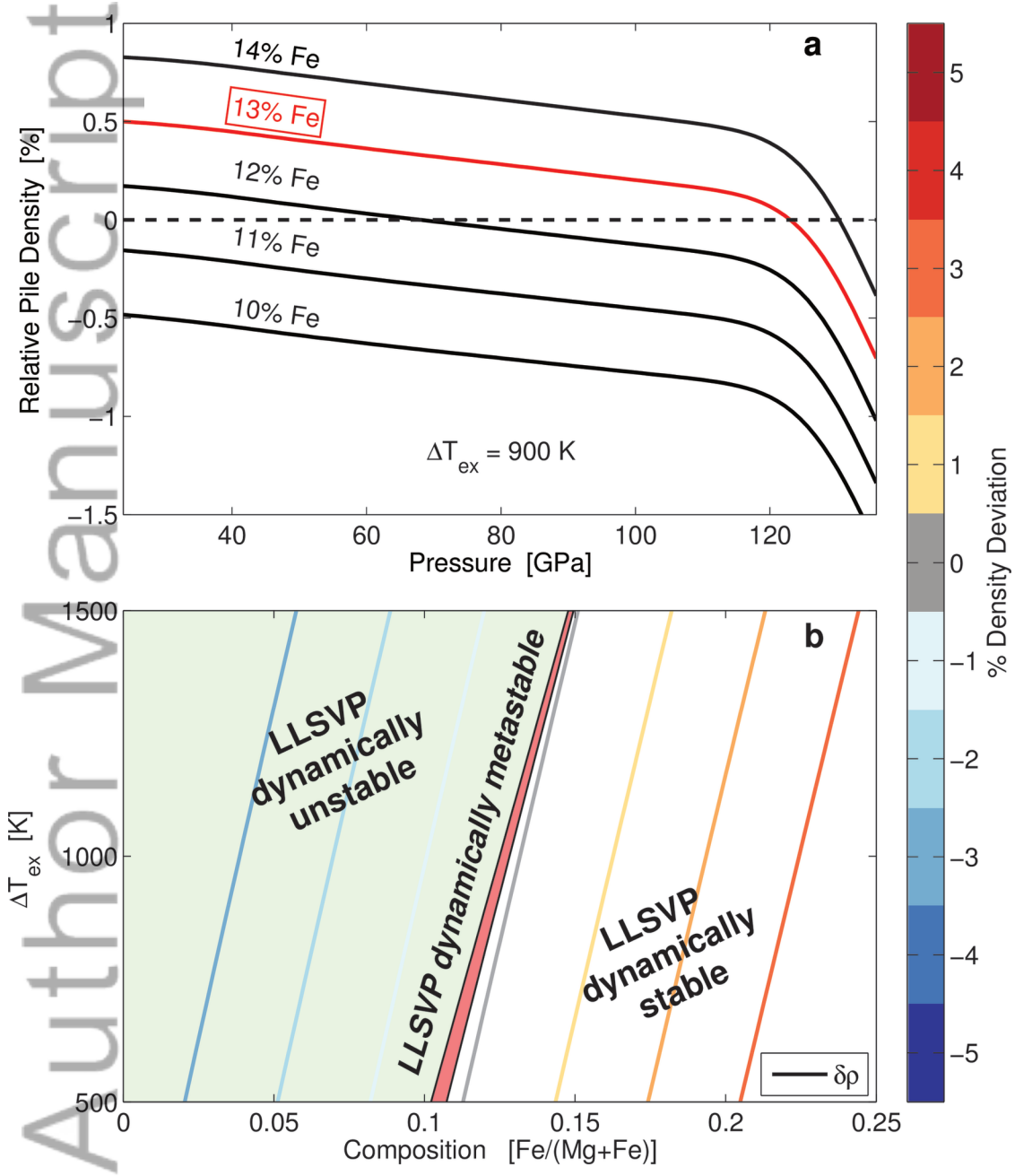

fig9